LIGHTNING STRIKES ON AIRBORNE GROUNDED SYSTEMS

A Dissertation

by

GILBERT APORU MALINGA

Submitted to the Office of Graduate and Professional Studies of
Texas A&M University
in partial fulfillment of the requirements for the degree of

DOCTOR OF PHILOSOPHY

Chair of Committee,	John Michael Niedzwecki
Committee Members,	Richard Orville
	Joseph Newton
	Ken Reinschmidt
Head of Department,	Robin Autenrieth

December 2014

Major Subject: Ocean Engineering

ABSTRACT

The modeling of lightning strike behavior and estimation of the subsequent electrical discharge is of great practical importance. In this study a complete two-dimensional physics based analytical formulation is presented for elevated grounded systems that can be envisioned to be contained within two non-concentric circular domains. The inner circle encompasses the body or system of interest and the periphery of the outer circle addresses the cloud coverage and ground surface. The potential field between the circular domains is modeled as the sum of two separate contributions. The first is formulated in terms of an eigen-function expansion involving simple radial functions and Legendre polynomials, while the second contribution is developed using two different approaches. The first approach utilizes an eigen-function expansion incorporating spherical Bessel functions and Legendre polynomials, while the second approach uses a Green's function formulation also involving orthogonal polynomial functions. Each of the contributions to the total potential field lead to linear systems of equations that are solved for the unknown series expansion coefficients. The accuracy of the potential field solution is investigated with regards to convergence, stability and error when compared with an exact solution. The potential field solution is then used as the basis to evaluate leader formation, regions of high risk, surface electrical charge and lightning collection area as a function of key parameters. The results indicate that the regions of high risk and surface electrical charge on an airborne structure are very sensitive to elevation, size of structure, cloud and leader parameters. The probability of lightning

attachment on the airborne structure was shown to increase with elevation and extent of cloud coverage and decrease with increase in diameter of the elevated structure. Further, the lightning collection area around the airborne structure was shown to increase with elevation and leader peak current. The electrical discharge, estimated using electrical current, is shown to be in the range of presently available data. The findings of this research study have practical implications for design and operation of tethered airborne systems.

ACKNOWLEDGEMENTS

This work was made possible by contributions from many people. First and foremost great appreciation is due to Prof. John Niedzwecki, my dissertation advisor, whose tireless commitment and encouragement provided impetus for this work. Through his guidance, I have developed a better appreciation for applied mathematics and the utility of probabilistic methods in highlighting the stochastic nature of certain physical phenomena. I would also like to thank members of my dissertation committee, Dr. Richard Orville, Dr. Joseph Newton and Dr. Ken Reinschmidt for providing technical insight to this work.

I gratefully acknowledge the financial support for this research work from the Wofford Cain'13 Senior Endowed Chair in Offshore Technology. I would also like to thank the Civil Engineering Department for providing additional partial financial support during the earlier stages of my graduate study at Texas A&M University.

I extend my deep gratitude to Prof. Zdenek Martinec at The Charles University in Prague for providing helpful suggestions on treatment of boundary value problems. Finally, I wish to thank friends and colleagues for their support during my time in graduate school. Special thanks go to Philip and Joyce Woodford, Sean Tolle, Sam Maopeng Fang, Susan Herlin, Wyatt Macgaffey, Don & Ann Foster, Ivan Felix, Yanbin Bai, Francisco Grajales, Madhuri Murali, Ajay Shastri, Ryan Beemer and Garrett Owens who have continually expressed interest in my work and have always served as a source of encouragement.

TABLE OF CONTENTS

Page

LIST OF FIGURES

Page

LIST OF TABLES

Page

1. INTRODUCTION

Background and Literature Review

Atmospheric science has provided a basic understanding of clouds and the sequence of atmospheric events leading to lightning or electrical discharges (Schonland, 1964; Uman, 1969; Rakov and Uman, 2003). The lightning process is preceded by buildup of electric charge in the thundercloud, which eventually leads to an electrical breakdown in the cloud creating a lightning discharge that propagates in a given direction. The destructive power of lightning discharges to both land-based and airborne systems that cannot adequately dissipate large impulses of energy is well documented (Miyake et al., 1990; Sorensen et al., 1998; Uman and Rakov, 2003). Lightning discharges can be either intracloud or cloud to ground discharges (Rakov and Uman, 2003). Intracloud lightning refers to the discharge of electric charge within cloud formations, while cloud to ground lightning involves the transfer of electrical energy between clouds and grounded structures. The later type of discharge can be divided into four different types depending on polarity of charge transferred and direction of leader propagation. Negative lightning transports negative charge from the cloud to ground while positive lightning carries positive charge from cloud to ground. Lightning can be further classified as downward or upward depending on direction of propagation and point of lightning initiation. Rakov and Uman (2003) report that negative downward lightning strikes account for 90 percent of cloud to ground strikes, while positive downward lightning strikes make up the remaining 10 percent.

Lightning propagating from a thundercloud towards a grounded body induces a potential field in the region surrounding the system or body. This potential field creates steep potential gradients in the immediate vicinity of the grounded body, which may lead to inception, and growth of upward leaders from the outer surface of the body. Leaders are ionized air that forms the basis for charge transferal of lightning strikes. The distance between the tip of the downward leader and grounded body at the instance the upward leader is incepted is known as the striking distance. The fastest traveling upward leaders have a high probability of intercepting the downward leader propagating from the thundercloud, providing a path for electric charge from the cloud to the ground surface. Depending on the atmospheric conditions leaders can travel several kilometers before attachment. The return stroke process commences when the upward leader intercepts the downward leader. This process involves transport of ground electric charge upward, neutralizing the charge deposited in the lightning channel and a fraction of that in the thundercloud (Krider, 1986; Rakov and Uman, 2003). Orville (1968) has reported that temperatures within a lightning channel can reach 30,000 K, that is over 53,500 ^{o}F, and the power dissipated according to Krider and Guo (1982) is on the order of 100 MW/m.

Airborne Systems

The types and applications of airborne concepts are varied and include lighter than air systems for energy generation (Altaeros, 2014), transportation (Aeroscraft, 2014), wireless communication (Google, 2014a) and surveillance (Raytheon, 2014). Airborne wind energy systems are deployed at high altitudes in order to extract power from the strong winds. These systems are tethered to the ground using a flexible cable. Thus,

substantially reducing the costs associated with the installation of more traditional land based or offshore wind turbine structural support structures. They are typically deployed at elevations in the range of 300 m to 4600 m, above the ground surface (Roberts et al., 2007). Fig. 1-1 illustrates the differences in distribution of the mean wind speed at different elevations above the mean water level. Several of these concepts have been demonstrated to be both technically feasible and easily deployable at remote locations (Fletcher and Roberts, 1979; O'Doherty and Roberts, 1982; Riegler and Riedler, 1983 and 1984; Furuya and Maekawa, 1984). Airborne wind systems can be relocated to adjust to seasonal variations in high altitude wind patterns, rendering the concept very attractive alternative to more traditional designs. Some alternative airborne concepts include the multi-rotor aerostat, and various tethered kite and flying airfoil designs (Roberts et al., 2007; Fagiano et al., 2010; Vermillion and Fagiano, 2013, Ahrens et al., 2014).

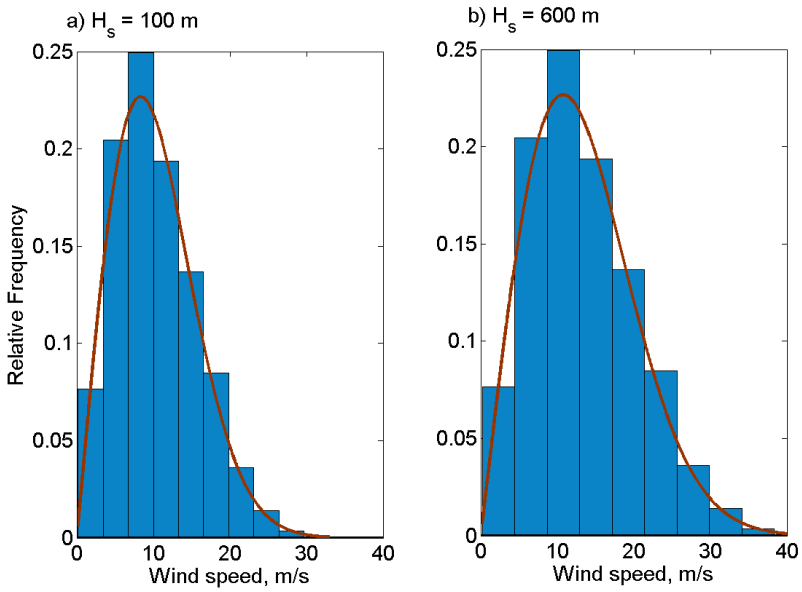

Fig. 1-1 Histogram of the average wind speed over a 10 year period at an elevation of a) $H_s = 100$ m and b) $H_s = 600$ m, above the mean water level at Montauk, New York. Wind data accessed from the National Buoy Data Center, NOAA, 2014.

Basically, all blimp-derived concepts are filled with gas to provide buoyant lift in air and are tethered to limit the motion at altitude and with respect to the base attachment point as illustrated in Fig. 1-2. The tether mooring an airborne wind turbine also serves to transmit the power generated to the base point where it is used or transmitted. Another very interesting concept for harvesting wind energy is the aerostat concept that incorporates 4 to 12 rotors units that provide lift and convert wind into electrical power through its tether line. It resembles a tethered streamlined flying helicopter. Other concepts include tethered kites and winged systems (an example is the Makani-Google airborne wind turbine, Google, 2014b), which generate power from the wind through their movement. Some concepts apply tension to a cable hooked to a generator on the ground

while others generate electrical power onboard and transmit it through the tether. A summary of the characteristics of several different airborne wind turbine system concepts is presented in Table 1-1. Other futuristic blimp-derived airborne platforms such as the vertical take-off vehicle used for heavy lifting operations, flying balloons for wireless communication and tethered aerostats for surveillance missions have also generated public interest. The leading developer for vertical take-off vehicles, Aeroscraft, has vehicles of different sizes, ranging from 81 m to 280 m in length and can operate at altitudes as high as 2900 m above the ground surface, and have a payload capacity of up to 500 tons (Aeroscraft, 2014). Prototypes for airborne telecommunication platforms are being developed to provide internet access to remote locations. An example is an array of solar powered untethered airborne balloons, 15 m in diameter and can fly at an altitude of up to 20,000 m above the ground surface, developed by Google to provide wireless access to remote locations in New Zealand (Brodkin, 2013; Google, 2014a). Traditionally, the United States military has relied on airships for conducting tactical surveillance operations in different parts of the globe. Recently, the United States Department of Defense has expressed interest in deploying a tethered airship, 74 m long and flying at an altitude of approximately 3000 m above the ground surface and operating for periods of up to 30 days, to provide critical information on targets of interest to national security on the U.S East Coast (Berkowitz et al., 2014; Raytheon, 2014).

Fig. 1-2 Schematic illustrating airborne wind turbines based on the concept of a tethered buoyant blimp (Altaeros, 2014).

Table 1-1 A summary of characteristics of existing airborne wind energy systems.

Developer	Concept	Capacity (MW)	Elevation (m)	Location
Altareos	Tethered blimp	0.03	150 - 600	Massachusetts
Makani Power	Aerostat	0.6	250 - 600	California
Joby Energy	Aerostat	2 - 5	150 - 600	California
Kitegen	Tethered airfoil	3 - 100	200 -1000	Italy

Studies show that tall structures are exposed to higher risk of lightning strikes (Eriksson, 1978; Golde, 1978; Anderson and Eriksson, 1980). The high risk of lightning strikes can be attributed to the intensification of the electric field, around tall structures, which increases with the elevation of structure, triggering upward lightning leaders, from the outer surface of the structure, which propagate towards the thundercloud. In addition, these structures are often placed in isolated environments posing higher risk of lightning strikes due to the greater intensification of the background electric field by the grounded structure. Therefore, the likelihood of lightning strikes on airborne systems can be high since these structures are often deployed at high elevations in isolated surroundings. Ji and He, (2013) show that lightning can attach to a transmission tether supporting an airborne wind turbine and thereby providing a path for electric energy that may destroy equipment on the ground if not adequately dissipated. However, the study is limited to lightning attachment on the tether line and no detailed investigation of lightning strikes to the entire airborne system is conducted. In addition, the latest International Electrotechnical Commission (IEC) design standards on lightning protection for wind turbines do not provide any guidance on assessing risk of lightning strikes on airborne wind systems. Therefore, need still exists to develop a better understanding of lightning behavior around airborne grounded systems operating under different environmental conditions.

Extreme Environmental Loads Caused by Lightning Strikes

The magnitude of the peak current and charge dissipated during a lightning strike to a grounded structure can be unusually large, posing the challenge of adequately dissipating the large impulse of energy as shown in the following studies. An investigation into the lightning behavior around elevated structures on the Swiss Alps showed that the peak current and charge dissipated during a lightning strike can exceed 200 kA and 350 C, respectively (Berger et al., 1975). In a different study, damage to tall structures on the West coast of Japan over a 9 year period, attributed to large impulses of energy in lightning strikes were observed (Miyake et al., 1990). In a follow up study, Miyake et al., (1992) measured the peak current and charge dissipated during lightning strikes to tall structures in the same region over a similar length of time as in the prior study. Their results show peak currents ranging from 2 to 100 kA and a maximum charge exceeding 3000 C, explaining the damage to structures in the prior study. Saba et al. (2010), in a study of lightning in Austria and the Americas, show an extensive dataset of duration and magnitude of peak current in lightning strikes. Based on the estimates of peak current and duration in that study, the magnitude of electric charge dissipated can exceed 2000 C.

Evidently, the maximum electric charge measured in all these studies exceeds the design threshold of 300 C recommended by IEC engineering standards for sizing lightning protection on grounded structures, implying need for additional work in order to develop a better understanding of lightning behavior and improved procedures for sizing lightning protection on elevated structures (IEC 2010a and IEC 2010b).

Theoretical Lightning Models

Earlier studies on lightning phenomenon used field data to develop empirical relationships relating geometric parameters to key lightning parameters (Berger, 1967; Golde, 1978; Anderson and Eriksson, 1980). It is evident that empirical models can be useful for preliminary design applications, however these models are inherently simplistic and often fail to capture the physics of lightning attachment to grounded structures. Although later theoretical models, developed to study lightning behavior around grounded structures, overcome some of the limitations of earlier empirical methods, these models are quite complex to implement and thus less practical for engineering applications (Bondiou and Gallimberti, 1994; Goelian et al, 1997). Other theoretical models such as the Rolling Sphere Method commonly utilized for sizing lightning protection on grounded structures because of its simplicity, faces a limitation of being unable to address the physics of leader inception and lightning attachment to grounded structures of complex geometry (Rizk, 1994; Szedenik, 2001; IEC, 2010a).

More recently Becerra and Cooray (2006) developed the physics based Self-consistent Leader Inception Model (SLIM) to address many of the limitations of earlier theoretical models. The model was formulated using the Poisson equation that governs the distribution of the electrical potential field around a grounded structure. Their model has been used to study the interaction of lightning with tall buildings and conventional wind turbines (Becerra et al., 2007; Becerra et al., 2008; Bertelsen et al., 2007; Madsen and Erichsen, 2009; Cooray and Becerra, 2012, Madsen et al., 2012). Table 1-2 illustrates a summary of the differences between the Rolling Sphere Method and the Self-consistent

Leader Inception Model. However, neither of these studies investigate lightning behavior around grounded structures deployed at high elevations above the ground surface. Preliminary studies indicate that structures operating at high elevations face increased risk of lightning, therefore need still exists to study the behavior of lightning around grounded elevated systems.

Table 1-2 Comparative summary of the models used for sizing lightning protection on grounded structures.

Model	Rolling Sphere Method	SLIM
Physics	Does not capture physics of leader inception and attachment to grounded complex structures	Adequately captures the physics of leader inception and attachment to all types grounded structures
Accuracy	Underestimates striking distances for tall structures. Cannot be used for sizing lightning protection on wind turbines blades	Estimates of striking distances and lightning protection zones are fairly accurate
Implementation	Less computationally intensive and fairly easy to apply	Computationally intensive but fairly easy to implement

The Poisson equation has traditionally been solved numerically using Finite Element method in past studies of lightning interaction with grounded structures (Becerra et al., 2007, Becerra et al., 2008; Madsen and Erichsen, 2009 and Madsen et al., 2012). However, the numerical schemes are fairly complex, computationally intensive and can be prone to large computational errors. The boundary value problem poised here can be solved using either an eigen-function expansion involving simple radial functions and

orthogonal polynomials or Green's function formulation. Since both formulations provide closed form solutions to the problem, this study exploits the advantages of each solution procedure, e.g. use of orthogonal relationships to compute boundary integrals and different methods of enforcing boundary conditions, by adapting a twofold approach involving an eigen-function expansion of special functions and Green's function to solve the Poisson problem and comparing the accuracy of each method. Therefore, a two-dimensional model based on the hybrid approach discussed above is developed to study lightning strike behavior on grounded elevated bodies enclosed within two non-concentric circles. The formulation and numerical solution developed in this study takes advantage of both the use of orthogonal polynomials and symmetry in the evaluation of the potential field.

Research Objectives

The main objectives of this work include:

- Develop a mathematical tool for evaluating the electrical potential field around grounded airborne systems subject to negative lightning strikes.
- Investigate the behavior of the potential field and corresponding regions of high risk, surface electrical charge and lightning collection areas around grounded elevated systems.
- Develop a computational tool for estimating electrical charge and energy dissipated during a lightning strike to a grounded structure.

In the first part of this research study, a mathematical formulation for the lightning boundary value problem is developed using an eigen-function expansion of special

functions and Green's solution. Then illustrative examples are presented to provide insight into the numerical stability and convergence properties of the solution scheme utilizing spectral concepts. Further, the solution scheme is validated using three different test cases with known analytical solutions. Numerical examples are used in the second part of the study to illustrate the behavior of the potential field and corresponding regions of high risk on grounded elevated bodies operating under different thundercloud conditions. The regions of high risk, which are represented using joint probability density functions, refer to probable areas for lightning attachment on the grounded structure. Further, the electrical charge induced on grounded airborne structures of different body shapes is investigated using illustrative examples. In addition, the study presents a semi-empirical method for estimating the extreme environmental loads such as the electrical charge and specific energy dissipated during a lightning strike to a grounded elevated structure. The last part of this research study investigates the striking distance, corresponding lightning collection area and strike frequency on the airborne structure. Striking distance bounds the lightning collection area around the grounded body and is used as a basis for design of lightning protection systems. Strike frequency is a measure of how often a grounded structure is struck by lightning in a given period. This frequency is a function of ground flash density, lightning collection area and distribution of lightning peak currents.

2. METHODOLOGY

A two-dimensional mathematical formulation based upon the Poisson equation is used to develop the total potential field around a grounded airborne structure. The domain of interest is represented by two non-concentric circles, where the inner circle defines the region that may contain one or more grounded bodies, while the outer circle represents the position of the thundercloud relative to the ground surface as illustrated in Fig 1-1. The essence of this physics-based model used to estimate the lightning field and its properties is presented in Fig. 2-1. The key aspects of the solution procedure are highlighted. These include the method of solution for the potential field based on an eigen-function expansion of special functions and Green's function, and the type of analyses conducted using the potential field around a grounded airborne structure. Parameters that include geometric information, cloud conditions and leader parameters are provided to the potential field module. The potential field solution is then efficiently computed from two contributions. The first is developed using an eigen-function expansion in terms of orthogonal polynomials that include Legendre functions and simple radial functions. The second contribution is evaluated using either spherical Bessel functions and Legendre polynomials or Green's function solution, and choice of the solution depends on the accuracy of the potential field as illustrated in section 2. The accuracy and convergence behavior of the potential field solution is investigated in the numerical stability module. A detailed characterization of the numerical solution is conducted using spectral concepts, and measures of numerical error and stability of the potential field solution are discussed,

as a function of the truncation limit and dimensionless offset distance of the inner circle, in section 3. The potential field solution is then used as the basis to evaluate leader formation, in the inception model module, as a function of geometrical, cloud and leader parameters. Regions of high risk to lightning strikes on the grounded structure are then developed, in terms of probability density functions, as a function of elevation, diameter of airborne structure, cloud and leader parameters. In addition, the surface electrical charge on the perimeter of airborne structures of different shapes is investigated using the total potential field in a separate module, and the results are presented as a function of elevation of structure, body geometry and environmental parameters. Further, the lightning striking distance is evaluated and forms the basis for determining lightning collection area, around the airborne structure, represented using probability density functions. Finally, the frequency of downward lightning strikes on the grounded airborne structure is evaluated as a function of elevation, diameter of structure and leader parameters.

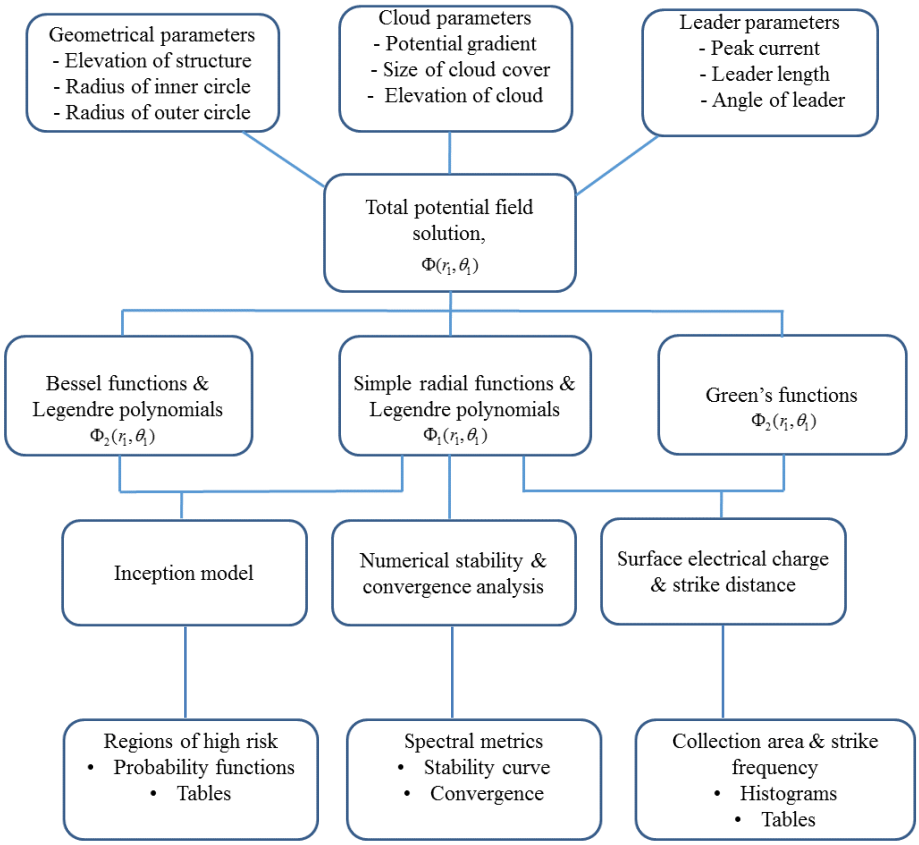

Fig. 2-1 Schematic showing the flow of information between the different modules in the lightning physics model.

Mathematical Formulation of Lightning Boundary Value Problem

The general form of the governing equation for the axially symmetric Poisson problem and the appropriate boundary conditions are given in Eq. (1). The problem, typically formulated in spherical coordinates has been reduced to the two-dimensional radially symmetric form that will be used to evaluate the electrical potential field in a region between two non-concentric circles (Asmar, 2005).

$$\begin{aligned} &\frac{\partial^2\Phi}{\partial r^2}+\frac{2}{r}\frac{\partial\Phi}{\partial r}+\frac{1}{r^2}\left(\frac{\partial^2\Phi}{\partial\theta^2}+\cot\theta\frac{\partial\Phi}{\partial\theta}\right) = f(r,\theta) \\ &r=[b,c], \quad \theta=[0,\pi] \\ &\Phi(b,\theta)=f(\mathrm{b},\theta), \quad \Phi(c,\theta)=f(c,\theta) \end{aligned} \tag{1}$$

where, Φ is the total potential function, b is radius of inner circle, c is radius of outer circle, $f(b,\theta)$ is the boundary condition specified on surface of inner circle and $f(c,\theta)$ is the cloud potential specified on surface of outer circle, taken as the product of the potential gradient at the base of the cloud and elevation of the cloud and $f(r,\theta)$ is the forcing function that characterizes the distribution of electric charge in the downward leader. The analytical formulation for the total potential field is then developed as a sum of two separate contributions. The first contribution is obtained by solving the Laplace problem with appropriate boundary conditions on the surface of the inner and outer circle. The second contribution is obtained by solving the Poisson problem with zero boundary conditions and a prescribed environmental forcing characterizing the distribution of electrical charge in the lightning downward leader (Cooray et al., 2007). The total potential field, $\Phi(\mathrm{r}_1,\theta_1)$ in the region between the two non-concentric circles is then

obtained as the sum of the two known potential functions in terms of the coordinates of the inner circle as shown in the following expression

$$\Phi(r_1, \theta_1) = \Phi_1(r_1, \theta_1) + \Phi_2(r_1, \theta_1) \quad (2)$$

The first term, $\Phi_1(r_1, \theta_1)$ in Eq. (2) is developed as an eigen-function expansion involving simple radial functions and Legendre polynomials. The second contribution, $\Phi_2(r_1, \theta_1)$ was formulated using two different approaches and the form selected depends upon the accuracy of the total potential field and type of analysis required, that is either regions of high risk or striking distance. The first approach involves an eigen-function expansion of spherical Bessel functions and Legendre polynomials that leads to a system of linear equations which are solved for unknown coefficients. The second method is based on an expansion of Green's function formulation also involving Legendre polynomials. The potential field solution involving the Bessel functions shows increased spreading, especially for line sources, but is accurate for practical applications when the downward leader is far from the grounded structure and therefore suitable for analysis involving regions of high risk on structures. On the other hand, the potential field solution based on Green's function shows realistic distribution of the field when the downward leader is close to the grounded structure and thus appropriate for striking distance calculations.

The formulation presented specifically allows vertical translation of the non-concentric inner circle, thus maintaining the problem symmetry about that axis. As illustrated in Fig. 2.2, the inner circle delimits a region around the periphery of either a

single body or an array of bodies of arbitrary shape. The inner region is contained within the second circular region whose upper boundary is used to specify the extent of the cloud cover.

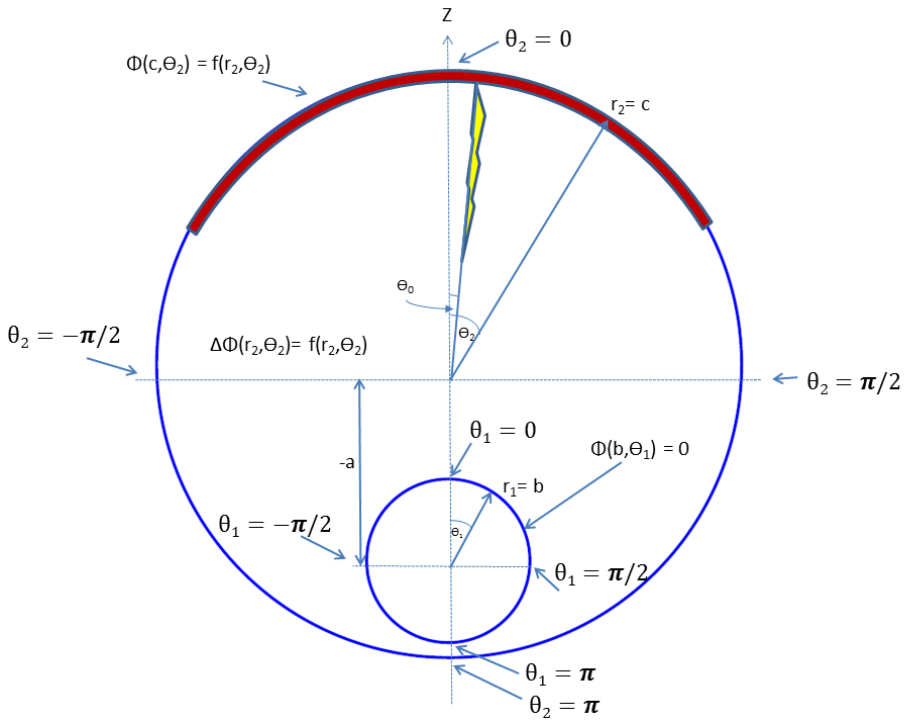

Fig. 2-2 Domain for the lightning problem with appropriate boundary conditions and environmental forcing.

Laplace Problem with Dirichlet Boundary Conditions

The problem can first be visualized as the evaluation of the potential field between two circles, where the potential field induced by the thundercloud on the boundary of the outer circle is governed by the Laplace's equation, which is a modified form of Eq. (1), noting that the forcing function is taken as zero in this case and the boundary conditions

remain unchanged. The potential function is then evaluated in the region between two circular domains as illustrated in Fig. 2-2, where a grounded inner circle is embedded within the larger circle, and the inner circle can enclose a single body or multiple bodies. Transforming the modified governing equation using separation of variables and a change of variables leads to two separate ordinary linear differential equations that can be recognized as the Euler equation and Legendre differential equation. Utilizing a coordinate transformation described in Appendix A, the general potential function solution can be expressed as a product of bounded solutions to the above differential equations in terms of the inner circle coordinates as

$$\Phi_1(r_1,\theta_1)=\sum_{n=0}^{N}\left[A_n\left(\frac{r_1}{c}\right)^n+B_n\left(\frac{c}{r_1}\right)^{n+1}\right]P_n(\cos\theta_1) \tag{3}$$

where, r_1 and θ_1 refer to the inner circle coordinate system, A_n and B_n are unknown modal coefficients of the radial Legendre series, and $P_n(\cos\theta_1)$ are Legendre orthogonal polynomial functions defined over the limits $[-1,1]$ consistent with the range of cosine of zenith angle, θ_1. Further, the inner circle can be moved upward or downward along the vertical axis and the variable a is used to represent the distance between centers of the inner and outer circles. It follows then that the range of the inner circle radii is $r_1=[b,r_c]$, where r_c is the radial extent of the surface of outer circle in coordinates of the inner circle. Upon substituting the boundary condition on the inner circle enables the general

solution to be expressed in terms of a single modal coefficient. Substituting the boundary condition on inner circle, $\Phi_1(\mathrm{b},\theta_1) = f(\mathrm{b},\theta_1)$ leads to the form

$$\sum_{n=0}^{N}\left[A_n\left(\frac{b}{c}\right)^n + B_n\left(\frac{c}{b}\right)^{n+1}\right]P_n(\cos\theta_1) = f(\mathrm{b},\theta_1) \tag{4}$$

Expanding this equation using Legendre polynomials and simplifying using orthogonal relationships yields an expression for the unknown coefficient, B_n in terms of the unknown coefficient, A_n and boundary integral, I_n which is then substituted into Eq. 3 leading to the following form of the potential function

$$\begin{aligned}
\Phi_1(r_1,\theta_1) &= \sum_{n=0}^{N}\left\{A_n\left[\left(\frac{r_1}{c}\right)^n - \left(\frac{b}{c}\right)^n\left(\frac{b}{r_1}\right)^{n+1}\right] + I_n\left(\frac{b}{r_1}\right)^{n+1}\right\}P_n(\cos\theta_1) \\
I_n &= \left(\frac{2n+1}{2}\right)\int_0^{\pi} f(\mathrm{b},\theta_1)P_n(\cos\theta_1)\sin\theta_1\, d\theta_1 \\
\left(\frac{2n+1}{2}\right) &= \int_0^{\pi}\left(P_n(\cos\theta_1)\right)^2\sin\theta_1\, d\theta_1
\end{aligned} \tag{5}$$

where, the modal coefficient, A_n, can be determined by applying the boundary condition at the surface of outer circle. The translation theorem, described in Appendix A, enables the rewriting of the solution in terms of the coordinates of outer circle such that the boundary condition on surface of outer circle can be applied. Substituting the expressions from the translation theorem into the potential function and rearranging terms leads to the form

$$\Phi_1(r_2,\theta_2)=\sum_{s=0}^{N}\left\{\left(\frac{r_2}{a}\right)^s\sum_{n=s}^{N}A_n\left(\frac{a}{c}\right)^n\left[\frac{(-1)^{n-s}n!}{s!(n-s)!}\right]-\left(\frac{a}{r_2}\right)^{s+1}\sum_{n=0}^{s}A_n\left(\frac{b}{c}\right)^n\left(\frac{b}{a}\right)^{n+1}\left[\frac{s!}{n!(s-n)!}\right]\right\}P_s(\cos\theta_2)$$
$$+\sum_{s=0}^{N}\left\{\left(\frac{a}{r_2}\right)^{s+1}\sum_{n=0}^{s}I_n\left(\frac{b}{a}\right)^{n+1}\left[\frac{s!}{n!(s-n)!}\right]\right\}P_s(\cos\theta_2) \tag{6}$$

The boundary condition on surface of outer circle is $\Phi_1(c,\theta_2)=f(c,\theta_2)$. Recognizing the symmetry of the problem, the range of $\theta_2=[0,\pi]$ and rewriting this equation at the outer surface of the circle and expanding the resulting form in terms of Legendre polynomials yields

$$\left\{\left(\frac{c}{a}\right)^s\sum_{n=s}^{N}A_n\left(\frac{a}{c}\right)^n\left[\frac{(-1)^{n-s}n!}{s!(n-s)!}\right]-\left(\frac{a}{c}\right)^{s+1}\sum_{n=0}^{s}A_n\left(\frac{b}{c}\right)^n\left(\frac{b}{a}\right)^{n+1}\left[\frac{s!}{n!(s-n)!}\right]\right\}\int_0^{\pi}\left(P_s(\cos\theta_2)\right)^2\sin\theta_2\,d\theta_2$$
$$+\left\{\left(\frac{a}{c}\right)^{s+1}\sum_{n=0}^{s}I_n\left(\frac{b}{a}\right)^{n+1}\left[\frac{s!}{n!(s-n)!}\right]\right\}\int_0^{\pi}\left(P_s(\cos\theta_2)\right)^2\sin\theta_2\,d\theta_2=\int_0^{\pi}f(c,\theta_2)P_s(\cos\theta_2)\sin\theta_2\,d\theta_2 \tag{7}$$

This can be rewritten in a more compact form using orthogonal relationships, leading to the form

$$\left\{\left(\frac{c}{a}\right)^s\sum_{n=s}^{N}A_n\left(\frac{a}{c}\right)^n\left[\frac{(-1)^{n-s}n!}{s!(n-s)!}\right]-\left(\frac{a}{c}\right)^{s+1}\sum_{n=0}^{s}A_n\left(\frac{b}{c}\right)^n\left(\frac{b}{a}\right)^{n+1}\left[\frac{s!}{n!(s-n)!}\right]\right\}\left(\frac{2}{2s+1}\right)$$
$$+\left\{\left(\frac{a}{c}\right)^{s+1}\sum_{n=0}^{s}I_n\left(\frac{b}{a}\right)^{n+1}\left[\frac{s!}{n!(s-n)!}\right]\right\}\left(\frac{2}{2s+1}\right)=F_s \tag{8}$$

By grouping various terms it is possible to write this even more compactly in matrix form as

$$\left(D_{sn} - E_{sn}\right) A_n + F_{sn} = F_s \tag{9}$$

where,

$$D_{sn} = a^{n-s} c^{s-n} \left[\frac{(-1)^{n-s}\, n!}{s!(n-s)!} \right] \left(\frac{2}{2s+1} \right) \qquad s = [0, N], \quad n = [s, N] \tag{10}$$

$$E_{sn} = a^{s-n} b^n \left(\frac{1}{c} \right)^s \left(\frac{b}{c} \right)^{n+1} \left[\frac{s!}{n!(s-n)!} \right] \left(\frac{2}{2s+1} \right) \qquad s = [0, N], \quad n = [0, s] \tag{11}$$

$$F_{sn} = a^{s-n} b^{n+1} \left(\frac{1}{c} \right)^{s+1} I_n \left[\frac{s!}{n!(s-n)!} \right] \left(\frac{2}{2s+1} \right) \qquad s = [0, N], \quad n = [0, s] \tag{12}$$

The matrix, F_{sn}, containing boundary terms from the surface of inner circle, is reduced to a column vector by summing along the rows to develop a new matrix, G_s which is compatible with matrix F_s which contains boundary terms from the surface of the outer circle. Finally, by recognizing the form of these matrices a further simplification, i.e. $C_{sn} = D_{sn} - E_{sn}$ and $f_s = F_s - G_s$ leads to obtaining a system of linear algebraic equations of the form

$$C_{sn}\, A_n \;=\; f_s \qquad\qquad s = [0, N], \quad n = [0, N] \tag{13}$$

This system of equations can be solved using for example the LU decomposition method (Borse, 1997) to evaluate the unknown modal amplitudes.

Poisson Problem with Zero Boundary Conditions

The second contribution to the total potential function, Φ_2, is developed in this section in a manner analogous to the previous section, but requires the solution of the Poisson's equation. Considering the situation of two non-concentric circles where the potential field induced by the lightning has the same form as Eq. (1) with zero boundary conditions on the surfaces of the inner and outer circle.

The forcing function, $f(r,\theta)$ representing the charge density in the lightning strike in volts can be expressed as

$$f(r,\theta)=\begin{cases}\dfrac{\rho(r_0,\theta_0)}{\varepsilon_0} & ;\theta=\theta_0\\ 0 & ;elsewhere\end{cases} \tag{14}$$

where, $\rho(r_0,\theta_0)$ is the charge distribution in the downward leader in Coulombs/m, ε_0 is the permittivity of free space in Farads/m, θ_0 is the angle of the downward leader, is given in Cooray et al. (2007) as

$$\begin{aligned}\rho(\mathrm{r}_0,\theta_0) &= A_0 I_{peak}\left(1-\frac{r_0-z_0}{H-z_0}\right)\times\left(1-\frac{z_0}{H}\right)+\frac{I_p\left(A+B\left(r_0-\mathrm{z}_0\right)\cos\theta_0\right)}{\left(1+C\left(r_0-\mathrm{z}_0\right)\cos\theta_0+D\left(\left(r_0-\mathrm{z}_0\right)\cos\theta_0\right)^2\right)}\\ &\times\left[0.3\exp\left(\frac{10-z_0}{75}\right)+0.7\left(1-\frac{z_0}{H}\right)\right]\end{aligned} \tag{15}$$

where, r_0 is the radial length along the leader in meters, z_0 is the elevation of the downward leader tip above the ground in meters, H is the elevation of the thundercloud in

meters, I_{peak} is the return stroke current in kilo-amperes, A_0, A, B, C and D are constants determined from field studies.

This boundary value problem can also be written as a Helmholtz equation in the form similar to Eq. 1, noting that the forcing can be expressed in the form, $f(r,\theta) = -k\Phi_2(r,\theta)$, where, k is a non-negative constant (Asmar, 2005). Using a similar approach as shown in the previous section, the solution of the Helmholtz equation is developed using separation of variables which leads to the spherical Bessel equation and Legendre differential equation. The general solution of this governing partial differential equation can be then expressed in terms of the coordinates of inner circle in spherical wave functions comprising bounded solutions to the spherical Bessel equation and Legendre differential equation (Arfken and Weber, 2005) as

$$\Phi_2(r_1,\theta_1) = \sum_{j=1}^{J_{\max}} \sum_{n=0}^{N_{\max}} \left[A_{jn}\ j_n(\lambda_{jn1} r_1) + B_{jn}\ y_n(\lambda_{jn1} r_1) \right]\ P_n(\cos\theta_1) \qquad (16)$$

where, $J_{\max}$ and $N_{\max}$ are the number of j and n terms in the general solution, respectively, A_{jn} and B_{jn} are the unknown modal coefficients associated with the general solution, and λ_{jn1} are roots of the first spherical Bessel function normalized by the radial extent of the outer circle. The spherical Bessel functions $j_n(.)$ and $y_n(.)$ are Bessel functions of the first and second kind, respectively, and $P_n(.)$ are Legendre orthogonal polynomial functions valid within the range of [-1, 1] in a manner consistent with the range of cosine of the zenith angle, θ_1. The general solution can be rewritten in terms of

a single set of modal coefficient upon substituting the boundary condition on the inner circle, $\Phi_2(\mathrm{b}, \theta_1) = 0$, and introducing roots of the second spherical Bessel function, λ_{jn2} to ensure that solution converges to the boundary condition on the surface of the outer circle, leading to the expression for the general solution as

$$\Phi_2(r_1, \theta_1) = \sum_{j=1}^{J_{\max}} \sum_{n=0}^{N_{\max}} A_{jn} \left[j_n(\lambda_{jn1}\, r_1) - \frac{j_n(\lambda_{jn1}\, b)}{y_n(\lambda_{jn2}\, b)}\; y_n(\lambda_{jn2}\, r_1) \right] P_n(\cos\theta_1) \quad (17)$$

where, the unknown set of coefficients associated with the general solution, A_{jn} can be determined from a relationship developed from a separate set of modal coefficients associated with the forcing function.

The charge source in the lightning problem can be treated as a line source and the corresponding forcing function can be then expressed in similar spherical wave functions with unknown modal coefficients associated with the forcing, C_{jn} as

$$\frac{\rho(r_0, \theta_0)}{\varepsilon_0} = \sum_{j=1}^{J_{\max}} \sum_{n=0}^{N_{\max}} C_{jn} \left[j_n(\lambda_{jn1}\, r_0) - \frac{j_n(\lambda_{jn1}\, b)}{y_n(\lambda_{jn2}\, b)}\; y_n(\lambda_{jn2}\, r_0) \right] P_n(\cos\theta_0) \quad (18)$$

Expanding the above equation in terms of spherical Bessel functions and then solving for modal coefficients of the line source, C_{jn} yields an equation of the form

$$C_{jn} = \frac{\dfrac{1}{\varepsilon_0} \displaystyle\int_b^{r_c} \rho(r_0, \theta_0)\, j_n(\lambda_{jn1}\, r_0) r_0^2 dr_0}{\left\{ \displaystyle\int_b^{r_c} \left[j_n^2(\lambda_{jn1}\, r_0) - \frac{j_n(\lambda_{jn1}\, b)}{y_n(\lambda_{jn2}\, b)}\, j_n(\lambda_{jn1}\, r_0) y_n(\lambda_{jn2}\, r_0) \right] r_0^2 dr_0 \right\} P_n(\cos\theta_0)} \quad (19)$$

In cases involving distributed charge sources, the modal coefficients can be determined in a similar manner by expressing the distributed forcing function in terms of spherical wave functions as shown by the following form

$$\mathrm{f}(r_0,\theta_0) \;\; = \sum_{j=1}^{J_{\max}} \sum_{n=0}^{N_{\max}} D_{jn} \left[j_n\left(\lambda_{jn1}\, r_0\right) - \frac{j_n\left(\lambda_{jn1}\, b\right)}{y_n\left(\lambda_{jn2}\, b\right)} \; y_n\left(\lambda_{jn2}\, r_0\right) \right] P_n(\cos\theta_0) \quad (20)$$

where, $\mathrm{f}(r_0,\theta_0)$ is the forcing function representing the distributed charge source and D_{jn} are modal coefficients of the distributed source.

Expanding the forcing function in terms of spherical Bessel and Legendre functions, and then solving for the modal coefficients associated with the distributed forcing function, D_{jn} leads to an equation of the solution for the modal coefficients associated with the distributed forcing function of the form

$$D_{jn} = \frac{(2n+1)}{2} \frac{\int_b^{r_c} \int_0^{\pi} f(r_0,\theta_0)\; j_n(\lambda_{jn1}\, r_0) P_n(\cos\theta_0) r_0^2 \sin\theta_0 \, d\theta_0 \, dr_0}{\int_b^{r_c} \left[j_n^2(\lambda_{jn1}\, r_0) - \frac{j_n(\lambda_{jn1}\, b)}{y_n(\lambda_{jn2}\, b)} \, j_n(\lambda_{jn1}\, r_0) y_n(\lambda_{jn2}\, r_0) \right] r_0^{\,2} dr_0} \quad (21)$$

Then using the relationship between the forcing function and the general solution developed earlier enables the modal coefficients of both the line and distributed forcing functions to be transformed into modal coefficients of the general solution, noting that the non-negative constant $k = \lambda_{jn1}^2$. It follows then that the modal coefficients of the general solution for the case of the line source can be determined from the following linear algebraic equations

$$A_{jn} = \lambda_{jn}^{-2} C_{jn} \qquad j = [1, \mathrm{J}_{\max}], \quad \mathrm{n} = [0, \mathrm{N}_{\max}] \tag{22}$$

The modal coefficients of the general solution for the distributed source can be determined in a manner analogous to the line source using similar linear algebraic equations with coefficients, C_{jn} replaced by D_{jn}.

Green's Expansion for Poisson Problem with Zero Boundary Conditions

The second contribution to the total potential function, Φ_2, is formulated in this section by developing a solution of the Poisson problem using Green's functions. The boundary conditions and range of coordinate parameters of the problem are analogous to those in the previous section. Green's formulation is based on the concept of developing a solution to a partial differential equation using a closed form function. This approach has been applied in past studies to solve problems involving point and line sources in hollow spherical domains (Morse and Feshbach, 1953; Jackson, 1999). This study extends the use of Green's function to solve problems involving line and distributed sources in concentric and non-concentric circular domains.

The general solution to the radially symmetric Poisson problem based on Green's formulation is given by the form (Jackson, 1999)

$$\Phi_2(\mathrm{r},\theta) = F \int_V \mathrm{f}(\mathrm{r}_0,\theta_0)\, G(\mathrm{r},\theta \mid \mathrm{r}_0,\theta_0)\, \mathrm{d}\Omega - \frac{1}{4\pi} \oint_S \left[\Phi_2(\mathrm{r}_0,\theta_0) \frac{\partial G(\mathrm{r},\theta \mid \mathrm{r}_0,\theta_0)}{\partial n_0} - G(\mathrm{r},\theta \mid \mathrm{r}_0,\theta_0) \frac{\partial \Phi_2(\mathrm{r}_0,\theta_0)}{\partial n_0} \right] dA_0 \tag{23}$$

where, $\Phi_2(r,\theta)$ is the potential field solution induced by a source at the observation point (r,θ) , F is a constant that depends on the type of potential field, $G(\mathrm{r},\theta\,|\,\mathrm{r}_0,\theta_0)$ is the Green's function, $\mathrm{f}(r_0,\theta_0)$ is the charge density of the source at a point (r_0,θ_0), V is total volume enclosed by boundary surface, S , $d\Omega$ is the volume element, n_0 is the outward unit normal to the boundary surface, $\Phi_2(r_0,\theta_0)$ is the potential field solution at a point on the boundary surface and dA_0 is the area of an element on S .

For a Poisson problem with zero boundary data, the boundary surface terms have no contribution to the potential field and the formulation reduces to the form

$$\Phi_2(\mathrm{r},\theta) = F\int_V \mathrm{f}(\mathrm{r}_0,\theta_0)\, G(\mathrm{r},\theta\,|\,\mathrm{r}_0,\theta_0)\,\mathrm{d}\,\Omega \tag{24}$$

Green's function is developed from solutions similar to those for the Euler equation and Legendre differential equation discussed previously. This time, the solutions are formulated using geometrical relationships as an infinite series involving radial functions and Legendre polynomials. The general form of the Green's function for grounded concentric circles containing a source in the region between the circles is given by the following modified form (MacRobert, 1967)

$$G(\mathrm{r},\theta \mid \mathrm{r}_0,\theta_0) = \frac{1}{R} - \sum_{n=0}^{N_{\max}} \left[1-\left(\frac{b}{c}\right)^{2n+1}\right]^{-1} \left\{ \frac{r_0^n}{r^{n+1}} \left[\left(\frac{r}{c}\right)^{2n+1} - \left(\frac{b}{c}\right)^{2n+1} \right] + \frac{b^n}{r_0^{n+1}} \left(\frac{b}{r}\right)^{n+1} \left[1-\left(\frac{r}{c}\right)^{2n+1}\right] \right\} P_n(\cos\alpha) \quad (25)$$

$$\frac{1}{R} = \sum_{n=0}^{N_{\max}} P_n(\cos\alpha) \begin{cases} \dfrac{r_0^n}{r^{n+1}} & ;\mathrm{r} > \mathrm{r}_0 \\ \dfrac{r^n}{r_0^{n+1}} & ;\mathrm{r} < \mathrm{r}_0 \end{cases}$$

where, $N_{\max}$ is the truncation limit, b is radius of inner circle, c is radius of outer circle, α is the angle between the position of the source, (r_0,θ_0) and a point of observation, (r,θ) and $P_n(.)$ are Legendre polynomials defined in the range consistent with the cosine of angle α. The Legendre polynomials, noting that the boundary value problem is radially symmetric, are given by the following relationship (Morse and Feshbach, 1953)

$$\mathrm{P}(\cos\alpha) = \mathrm{P}(\cos\theta_0)\,\mathrm{P}(\cos\theta) \quad (26)$$

The lightning problem can be treated as a line source, with a uniform charge density, q in units of Coulombs/m, computed from the electric charge distribution function described using Eq. (15). This ensures that the treatment of the radial integral in the general solution is tractable. Therefore, the expression for the line source is, $f(r_0,\theta_0) = q$, the constant associated with electrostatic potential fields is given by, $F = (4\pi\varepsilon_0)^{-1}$ and noting that $r_0 = z$ is a point on the line source, the potential field

solution in the region between two grounded circles is then developed by solving the line integral of the product of the forcing and Green's function as given by the form

$$\Phi_2(\mathrm{r},\theta) = \frac{q}{4\pi\varepsilon_0}\sum_{n=0}^{N_{\max}}\left\{\int_b^c G(\mathrm{r}\,|\,\mathrm{r}_0)\,\mathrm{dz}\right\}\mathrm{P}_n(\cos\theta_0)\,\mathrm{P}_n(\cos\theta)$$

$$G(\mathrm{r}\,|\,\mathrm{r}_0) = \frac{1}{R_n} - \left[1-\left(\frac{b}{c}\right)^{2n+1}\right]^{-1}\left\{\frac{z^n}{r^{n+1}}\left[\left(\frac{r}{c}\right)^{2n+1} - \left(\frac{b}{c}\right)^{2n+1}\right] + \frac{b^n}{z^{n+1}}\left(\frac{b}{r}\right)^{n+1}\left[1-\left(\frac{r}{c}\right)^{2n+1}\right]\right\} \quad (27)$$

$$\frac{1}{R_n} = \begin{cases} \dfrac{z^n}{r^{n+1}} & ;\mathrm{r} > \mathrm{z} \\ \dfrac{r^n}{z^{n+1}} & ;\mathrm{r} < \mathrm{z} \end{cases}$$

The integral in Eq. (27), can be subdivide into two separate integrals. The first integral, represents the source contribution from the range, $b \le z < r$ while the second integral, addresses the source contribution from the range, $r \le z \le c$. Solving the first and second integral and summing the resulting integrand and substituting in Eq. (27) leads to the following expression for the potential function

$$\begin{aligned}\Phi_2(\mathrm{r},\theta) = \frac{q}{4\pi\varepsilon_0}\sum_{n=0}^{N_{\max}}\Bigg\{&\frac{1}{n}\left[1-\left(\frac{r}{c}\right)^n\right] + \frac{1}{n+1}\left[1-\left(\frac{b}{r}\right)^{n+1}\right] - \left[1-\left(\frac{b}{c}\right)^{2n+1}\right]^{-1}\Bigg\{\frac{1}{n}\left[1-\left(\frac{b}{c}\right)^n\right] \\ &\times\left(\frac{b}{r}\right)^{n+1}\left[1-\left(\frac{r}{c}\right)^{2n+1}\right] + \frac{1}{n+1}\left[\left(\frac{r}{c}\right)^{2n+1} - \left(\frac{b}{c}\right)^{2n+1}\right]\left[\left(\frac{c}{r}\right)^{n+1} - \left(\frac{b}{r}\right)^{n+1}\right]\Bigg\}\Bigg\} P_n(\cos\alpha)\end{aligned} \quad (28)$$

The potential field solution is undefined for $n = 0$, thus the general solution is modified to ensure that the solution is determinate for each of the terms in the summation. The indeterminate terms can be eliminated by computing the total integral at $n = 0$ and

adding the result to the general solution. After applying a coordinate transformation, the potential field contribution for a region between two non-concentric circles, in coordinates of the inner circle, is given by the form

$$\Phi_2(\mathrm{r}_1,\theta_1)=\frac{q}{4\pi\varepsilon_0}\left\{In\left(\frac{r_c}{r_1}\right)+\left(1-\frac{b}{r_1}\right)-\left[1-\frac{b}{r_c}\right]^{-1}\left\{\left(\frac{b}{r_1}\right)\left[1-\frac{r_1}{r_c}\right]In\left(\frac{r_c}{b}\right)+\left(1-\frac{b}{r_1}\right)\left(1-\frac{b}{r_c}\right)\right\}+\right.$$
$$\sum_{n=1}^{N_{\max}}\left\{\frac{1}{n}\left[1-\left(\frac{r_1}{r_c}\right)^n\right]+\frac{1}{n+1}\left[1-\left(\frac{b}{r_1}\right)^{n+1}\right]-\left[1-\left(\frac{b}{r_c}\right)^{2n+1}\right]^{-1}\left\{\frac{1}{n}\left[1-\left(\frac{b}{r_c}\right)^n\right]\left(\frac{b}{r_1}\right)^{n+1}\right.\right. \quad (29)$$
$$\left.\left.\times\left[1-\left(\frac{r_1}{r_c}\right)^{2n+1}\right]+\frac{1}{n+1}\left[\left(\frac{r_1}{r_c}\right)^{2n+1}-\left(\frac{b}{r_c}\right)^{2n+1}\right]\left[\left(\frac{r_c}{r_1}\right)^{n+1}-\left(\frac{b}{r_1}\right)^{n+1}\right]\right\}\right\}\right\}P_n\left(\cos\alpha_1\right)$$

where, r_c is the radial extent of the surface of the outer circle in coordinates of the inner circle and α_1 is the angle between a point on the source, (r_0,θ_0) and a point of observation, (r_1,θ_1), and the Legendre polynomial is of the form shown in equation (26).

In the case of a distributed source, the potential field solution in the region between two grounded concentric circles is developed by computing the volume integral of the product of the forcing and Green's function as given by the following form

$$\Phi_2(\mathrm{r},\theta)\ =2\pi F\sum_{n=0}^{N_{\max}}\left\{\int_b^c\int_0^\pi \mathrm{f}(\mathrm{r}_0,\theta_0)\,G(\mathrm{r}\,|\,\mathrm{r}_0)\,\mathrm{P}_n(\cos\theta_0)\sin\theta_0\,r_0^2\,d\theta_0\,dr_0\right\}\mathrm{P}_n(\cos\theta) \quad (30)$$

where, the constant 2π is the integrand with respect to the azimuthal angle, ϕ_0. Treatment of the radial integral in this case follows a similar approach as that shown in the derivation of the potential field solution for the line source. The integral involving the zenith angle,

θ can be solved numerically and the constant in the general solution is taken to have a value of unity.

Upward Leader Inception Model

Once the radially symmetric potential field is evaluated, the relevant equations for lightning strikes propagating from the cloud to a structure can be characterized. A schematic of the evaluations that are preformed determine inception of positive upward leaders once the total potential field has been solved is presented in Fig. 2-3. This evaluation process begins at the upper most point on the perimeter of the inner circle and proceeds around the enclosed body until a position is reached where the downward leader tip is beyond line of sight. The process is repeated for a range of downward leader angles deemed feasible from literature on lightning-structure interaction (Armstrong and Whitehead, 1968; Miyake et al., 1990).

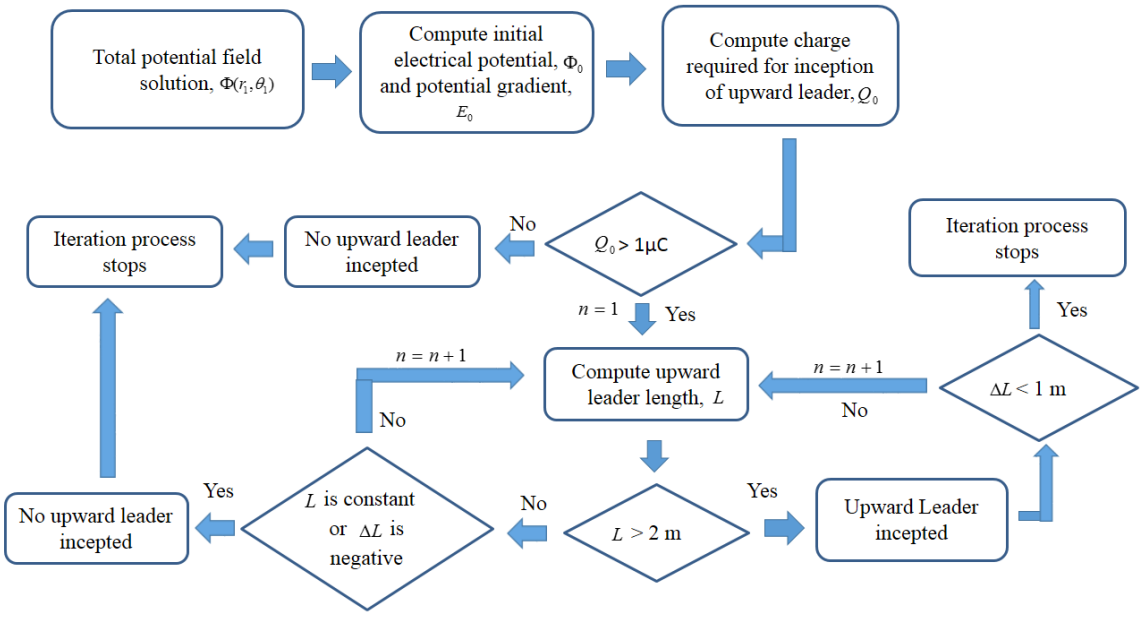

Fig. 2-3 Schematic illustrating the algorithm used for determining positive upward leader growth from a specific point on the perimeter of the inner circle.

The inception of a positive upward leader from the perimeter of the inner circle can be estimated using semi-empirical the relationships presented by Becerra and Cooray. (2006). The potential field surrounding the body is used in estimating the growth of the upward leader. The vertical distribution of the potential field between a given point on the perimeter of the inner circle and position of the downward leader tip is used to determine the initial charge available for inception of an upward leader. Due to differences in spatial resolution of the potential field solution, the required vertical distribution of the potential field between each point on the outer surface of inner circle and position of the downward leader tip is interpolated from the total potential field. A linear fit of the

corresponding potential field is then used to estimate the initial electrical potential and the potential gradient required to compute the initial charge available for upward leader inception. The potential field between a point on the perimeter of the grounded structure and location of downward leader tip, and the initial charge available for upward leader inception are evaluated using the following relationships

$$\begin{aligned} \Phi(z) &= E_0 z + \Phi_0 \\ Q_0 &= \frac{K_Q \Phi_0^{\,2}}{2(E_s - E_0)} \end{aligned} \tag{31}$$

where, $\Phi(z)$ is the vertical distribution of the potential field between a given point on the perimeter of the grounded structure and position of downward leader tip in volts, E_0 is the initial potential gradient in volts/m, z is the vertical distance above a given point on body in meters, Φ_0 is the initial electrical potential in volts, Q_0 is the initial charge available for upward leader inception in Coulombs, K_Q is a geometrical constant that relates electrical potential to charge in the region around the tip of an incipient upward leader in Coulombs/meters and, E_s is the positive gradient of streaming electric arcs in the region around the tip of incipient upward leader in volts/m. The geometrical constant and positive streamer gradient are determined from field studies of lightning (Becerra and Cooray, 2006).

When the initial charge exceeds a minimum threshold of 1 μCoulomb, the iterative process of computing the length of the upward leader, at a given point on the periphery of the grounded body, commences with the iteration step, $n = 1$, noting that the initial upward

leader length is assumed to be a few centimeters, typically 5 cm. The new length of the upward leader is computed using the following equations

$$\begin{aligned} L^{n+1} &= L^n + \Delta L^n \\ \Delta L^n &= \frac{\Delta Q^n}{q_L} \end{aligned} \tag{32}$$

where, L^n is the upward leader length at the n^{th} iteration step in meters, ΔL^n is the incremental upward leader length in meters, ΔQ^n is the charge contained within the region around the tip of upward leader at the n^{th} iteration step in Coulombs, this charge drives the growth of the leader and q_L is the charge per unit length in Coulombs/meter, required in the thermal transition process of the upward leader and is determined from field studies (Becerra and Cooray, 2006). The charge contained within the zone around the tip of upward leader, ΔQ^n and electrical potential at the tip of the incipient upward leader in volts, Φ_T^n at the n^{th} iteration step, are computed using the following semi-empirical relationships

$$\begin{aligned} \Delta Q^n &= K_Q \left\lfloor \left(E_s \left(L^n - L^{n-1} \right) + \Phi_T^{n-1} - \Phi_T^n \right) \left(l_s^{n-1} - L^n \right) \right\rfloor \\ \Phi_T^n &= E_c L^n + x E_c In \left[\frac{E_s}{E_c} - \left(\frac{E_s}{E_c} - 1 \right) \exp\left(-\frac{L^n}{x} \right) \right] \end{aligned} \tag{33}$$

where, l_s^n is the length of streaming electric arc propagating from region around tip of upward leader, in meters, E_c is the final quasi-stationary leader potential gradient in volts/m, x is a constant in meters, given by the product of upward leader speed and leader

time constant. The final quasi-stationary leader potential gradient, upward leader speed and leader time constant are determined from field studies (Becerra and Cooray, 2006). The upward leader length preceding the initial leader length, L^0 is very small and can be taken as zero. The initial electrical potential at the tip of the incipient upward leader, Φ_T^0 is equivalent to Φ_0. The first streamer length, l_s^0 and streamer length, l_s^n in the n^{th} iteration step are given as

$$\begin{aligned} l_s^0 &= \frac{\Phi_0}{E_s - E_0} \\ l_s^n &= l_s^0 + \frac{E_s L^n - \Phi_T^n}{E_s - E_0} \end{aligned} \tag{34}$$

In cases where the minimum charge threshold of 1 μCoulomb is not met at a specific point on the surface of grounded body, upward leader inception is not possible at that location. The computation process ceases and the algorithm proceeds to the next point on the surface where the entire iterative process is repeated.

A stable upward leader is assumed to develop from the perimeter of the grounded structure once the leader length exceeds a designated threshold, usually 2 m, otherwise no inception of upward leader is assumed to occur. For cases where successful inception occurs, the iterative process of computing leader length stops when the incremental leader length between two preceding iterations is minimal, typically less than a meter. The points on the periphery of the structure where the inception of upward leaders occur are probable attachment locations for the downward leader, therefore the spatial distribution of these points, represented using the normal bivariate probability density function shown in

Appendix B, delimit the region of high risk on the structure. Similar criteria can be utilized to study upward triggered lightning from the grounded structure in absence of a distinct downward leader. In this case, the potential field is induced by only the thundercloud, and positive upward leaders are incepted from the perimeter of the structure when the background potential field meets the threshold for leader inception.

Surface Electrical Charge on Grounded Structures of Different Geometry

The electrical charge, Q_b in Coulombs, induced on the perimeter of a cylindrical grounded structure is computed from the total potential field by using the following form

$$Q_b = D\,L\,\varepsilon_0 \int_0^{\pi} \frac{d\Phi(\mathrm{b},\theta_1)}{dr_1}\, d\theta_1 \tag{35}$$

where, $\Phi(\mathrm{b},\theta_1)$ is the total potential field on the perimeter of the structure, D is the diameter of the structure in meters, L is the length of the structure in meters, b is the radius of the structure, r_1 is the radial coordinate in terms of coordinates of the inner circle, θ_1 is the angular coordinate and ε_0 is the permittivity of free space in Farads/m.

Assuming the angular variation of the potential gradient on the perimeter of the structure can be approximated as the mean potential gradient along the surface of the structure, $E_{avg}(\mathrm{D})$. Then the electrical charge induced on the outer surface of the structure is given by the form

$$Q_b = \pi D\,L\,\varepsilon_0 E_{avg}(D) \tag{36}$$

The electrical charge on the perimeter of structure can be normalized by dividing with the surface area of the structure leading to the following expression for the normalized electrical charge, Q_s

$$Q_s = \varepsilon_0 E_{avg}(D) \tag{37}$$

The total normalized surface electrical charge, Q_t in Coulombs/m, on grounded structures of different geometric shapes can be determined by discretizing the structure into small cylindrical elements of different diameter and computing the corresponding surface charge on each element using simple quadrature as given by the following expression

$$Q_t = h\sum_{i=1}^{N} Q_s(D[i]) \tag{38}$$

where, h is the length of the cylindrical element, $D[i]$ is diameter of the element and N is the total number of elements. Alternatively, the total normalized surface charge can be determined numerically using the following equation

$$Q_t = \int_0^L Q_s(\mathrm{x})\,\mathrm{d}x \tag{39}$$

where, $Q_s(\mathrm{x})$ is a function that relates electrical charge on the structure to length, x along the grounded structure.

Environmental Loads Induced by Lightning

The total charge transferred during a lightning strike to an elevated grounded structure occurs after the downward leader intercepts the upward leader during the return stroke process which involves the transfer of electrical charge between the thundercloud and the ground, through the elevated structure. The charge dissipated is composed of two parts, the first contribution is the electrical charge in the short stroke process where the impulsive transfer of charge occurs between the thundercloud and the ground surface through the elevated structure, the duration of the process is short, typically $1.0\,ms$. The second contribution is the charge dissipated during the long stroke process which is characterized by flow of long duration electrical current through the elevated structure to the ground surface. The magnitude of the total charge dissipated during a lightning strike to a grounded structure can be computed as the integral of the wave forms for the electrical current in both the short and long stroke processes as shown by the following expression

$$Q = \int_0^{t_{short}} I_{short}(t)\,dt + \int_0^{t_{long}} I_{long}(t)\,dt \tag{40}$$

where, Q is the total charge dissipated during a lightning strike in Coulombs, $\mathrm{I}_{short}(\mathrm{t})$ is the short stroke current in amperes, $\mathrm{I}_{long}(\mathrm{t})$ is the long stroke current in amperes, t_{short} is the duration of the short stroke and t_{long} is the duration of the long stroke in seconds.

The specific energy, E dissipated during a lightning strike is computed using the following equation

$$E = \int_0^{t_{short}} I_{short}^2(t)\,dt + \int_0^{t_{long}} I_{long}^2(t)\,dt \tag{41}$$

The short stroke current is represented using Heidler functions of the form in IEC 62305-1 as shown by the following equation (IEC, 2010b)

$$I_{short}(t) = \frac{I_{speak}}{k_f}\left[\frac{\left(\frac{t}{\tau_1}\right)^{10}}{1+\left(\frac{t}{\tau_1}\right)^{10}}\right]\exp\left(-\frac{t}{\tau_2}\right) \tag{42}$$

where, I_{speak} is the short stroke peak current in amperes, k_f is the correction factor for the amplitude of the short stroke peak current and is determined from a parametric analysis, t is the time in seconds, τ_1 is the front time constant, representing the ascending portion of the wave form and τ_2 is the tail time constant in seconds, which defines the extent of the decaying portion of the current wave. The estimates for the correction factor, front time and tail time constants are given in IEC 62305-1.

The current wave form for the long stroke current is assumed to be similar to a tapered square wave and the form can be represented using a filter function utilized by Roberts and Roberts, (1978) for a different application, and modified to suit the needs of this study as shown by the following form

$$
\begin{aligned}
I_{long}(t) &= I_{lpeak} \lfloor f_1(t) + f_2(t) \rfloor \\
f_1(t) &= \left[1 + \left(\frac{t_{long} - t}{t_{long} - t_{front}} \right)^{2k_{long}} \right]^{-0.5} \quad , 0 \le t \le t_{front} \\
f_2(t) &= \left[1 + \left(\frac{t}{t_{tail}} \right)^{2k_{long}} \right]^{-0.5} \quad , t_{front} < t \le t_{long}
\end{aligned}
\tag{43}
$$

where, I_{lpeak} is the long stroke peak current in amperes, $f_1(t)$ and $f_2(t)$ are functions that characterize the shape of the current wave form, k_{long} is a dimensionless shape parameter that controls the gradient of the rising and decaying portions of the wave form, t_{front} is the duration of the rising portion of the current wave form and t_{tail} is the time the current starts to decay.

The filter function can be modified to represent a range of shapes for the current wave form by adjusting the shape parameter, and the duration of the rising and decaying current. The resulting probable shapes for the current include triangular, parabolic and tapered square wave forms. In this study, the long stroke current is represented as a tapered square wave form. The short stroke process in the numerical example shown later, is assumed to comprise of a single stroke with a duration of $1.0\,ms$. The total duration of the current in the long stroke processes was assumed as 50 ms, and the corresponding duration for the front current and start time for the tail current were taken as 10 and 90 percent of the total duration, respectively. The mean and standard deviation of the peak current in both the short and long stroke processes, that is I_{speak} and I_{lpeak}, respectively were selected to reproduce a range of typically observed peak currents in lightning strikes

as shown in (Berger et al., 1975 and Saba et al., 2010), using a random number generator based on the log normal probability distribution.

Striking Distance, Lightning Collection Area and Strike Frequency

The striking distance, defined as the distance between the tip of the downward leader and perimeter of a grounded structure at the instance an upward leader is incepted, provides the basis for computing the lightning collection area and frequency of strikes to a grounded structure. The lightning collection area around a grounded structure is defined as the equivalent area on the ground surface exposed to lightning strikes. The strike frequency is the number of lightning strikes to a structure within a defined period. The striking distance which is a function of the peak current in the downward leader, elevation and diameter of the grounded structure, is computed utilizing the total potential field, and is assumed to be reached when the mean potential gradient between the perimeter of the grounded structure and tip of downward leader is approximately 500 kilo-volts/m.

The lightning collection area around the grounded structure, A_c is computed as the circumferential area defined by the striking distance. The collection area which is normalized by dividing with the area of the grounded structure, A_b is represented as a function of the probability distribution of the lightning peak current in the downward leader which is determined randomly using a number generator in order to reproduce a range of peak currents commonly observed in nature as reported in Saba et al., 2010. The lightning strike frequency, N_s is computed as a function of the ground flash density, N_g which is the number of lightning strikes to the bare ground surface, lightning collection

area and the cumulative probability distribution of the leader peak current. The frequency of lightning strikes to the grounded structure is then given by the following expression

$$N_s = N_g A_c \int_{I_{\min}}^{I_{\max}} f(I_{peak})\, dI_{peak} \tag{44}$$

where, $I_{\min}$ and $I_{\max}$ are the lower and upper bound of the downward leader peak, I_{peak} , and $f(I_{peak})$ is the probability density function of the leader peak current.

The skewness and kurtosis of the probability distribution of the lightning collection area are investigated. The skewness parameter, s_k is a measure of asymmetry of the probability distribution and is given by the form (Ang and Tang, 1975)

$$s_k = \frac{E(\mathrm{x}-\mu)^3}{\sigma^3} \tag{45}$$

where, x is the random variable, μ is the mean value and σ is the standard deviation of the random variable. Kurtosis, k_t defines the characteristics of the peak of the probability distribution and is given by the form

$$k_t = \frac{E(\mathrm{x}-\mu)^4}{\sigma^4} \tag{46}$$

3. NUMERICAL STABILITY, CONVERGENCE AND MODEL VALIDATION

Characterization of Numerical Solution

The accuracy and numerical stability of the potential field solution are a concern from both an analytical and a practical point of view, and are investigated using spectral concepts. The solution schemes to the Poisson problem, with zero boundary data, involving spherical Bessel functions and Green's function are stable for the range of model parameters considered in this study. Therefore, the numerical stability study conducted here focuses solely on the accuracy and stability of the potential field solution to the Laplace problem with different boundary conditions on the inner and outer circle. The system of linear equations to the Laplace problem can be rewritten as $AX = B$, where A is a square coefficient matrix of size $N_{\max} + 1$, X is the corresponding vector of modal coefficients and B is a vector containing boundary terms. In all the analyses that follow, the inner circle is assumed to be grounded, therefore the B term in the expression for the linear system of equations contains only boundary terms from the outer circle.

The accuracy and numerical stability of the potential field solution is affected by the geometry of solution domain and truncation limit. The distance between the centers of the inner and outer circle, also known as the offset distance, a defines the pattern and conditioning of the coefficient matrix and thus has a direct bearing on the accuracy and numerical stability of the potential field solution. When the offset distance, $a = 0$, the inner and outer circles are concentric and the coefficient matrix is sparse and can be easily invertible. However, when the offset distance is greater than zero, the circles are non-

concentric and the coefficient matrix is fully populated and can be difficult to invert. The truncation limit defines the size of the coefficient matrix, thus indirectly affects the conditioning of the matrix which in turn has an effect on the accuracy and numerical stability of the potential field solution.

Spectral Analysis

The impact of the offset distance and truncation limit on accuracy and numerical stability of potential field solution is investigated in detail by exploring the distribution of the condition number of the coefficient matrix, $K(A)$, which is used here to measure the transfer of error from the coefficient matrix, *A*, and vector of boundary terms, *B* to the vector of modal coefficients, *X*. Generally, large condition numbers imply large error in the solution. Matrices can also be classified into two categories as normal and non-normal. A normal matrix has orthogonal eigenvectors and therefore can be diagonalizable. On the other hand, a non-normal matrix has non-orthogonal eigenvectors (Trefethen, 1992; Trefethen and Embree, 2005). Normality or non-normality can also be defined based on condition number. In cases where the condition number is large, the matrix can be highly non-normal and its eigenvalues sensitive to perturbations. The ill-conditioning in highly non-normal matrices can pose problems for algorithms designed to solve linear system of equations and thus introducing error or numerical instability in the solution as shown later.

Fig. 3-1a was developed to illustrate the relationship between the offset distance and optimal number of terms in general solution required for adequate convergence and stability of potential field solution from the first contribution, $\Phi_1(r_1, \theta_1)$. Convergence is

considered adequate if the potential field solution at the boundary matches the prescribed boundary condition. Fig. 3-1b shows the distribution of condition numbers of the coefficient matrix for different offset distances and truncation limits. Generally, the optimal truncation limit is shown to decrease with increase in offset distance along a similar range of condition numbers. For small offset distances, $a \leq 0.2$, the solution scheme is numerically stable for a large range of truncation limits and the error in the potential field solution is bounded. In contrast, offset distances in the range $a > 0.2$ produce highly non-normal matrices with condition numbers that increase exponentially with the truncation limit, implying that numerical stability and error in the potential field solution from the first contribution can grow at a similar pace. The size of the error is magnified as the inner circle moves closer to the boundary of the outer circle.

The effect of varying the truncation limit, for a case where the offset distance, $a = 0.9$ on quality of the potential field solution from the first contribution is illustrated in Fig. 3-2a and Fig. 3-2b. This example demonstrates that increasing the number of terms in the general solution, $N_{\max}$ beyond the optimal number can lead to significant error in computing the potential field as shown in Fig. 3-2b. It is evident that increasing $N_{\max}$ does not always improve the quality of the numerical solution. Due to symmetry of the problem, the trends in condition numbers and convergence behavior discussed above are similar for both positive and negative offset distances.

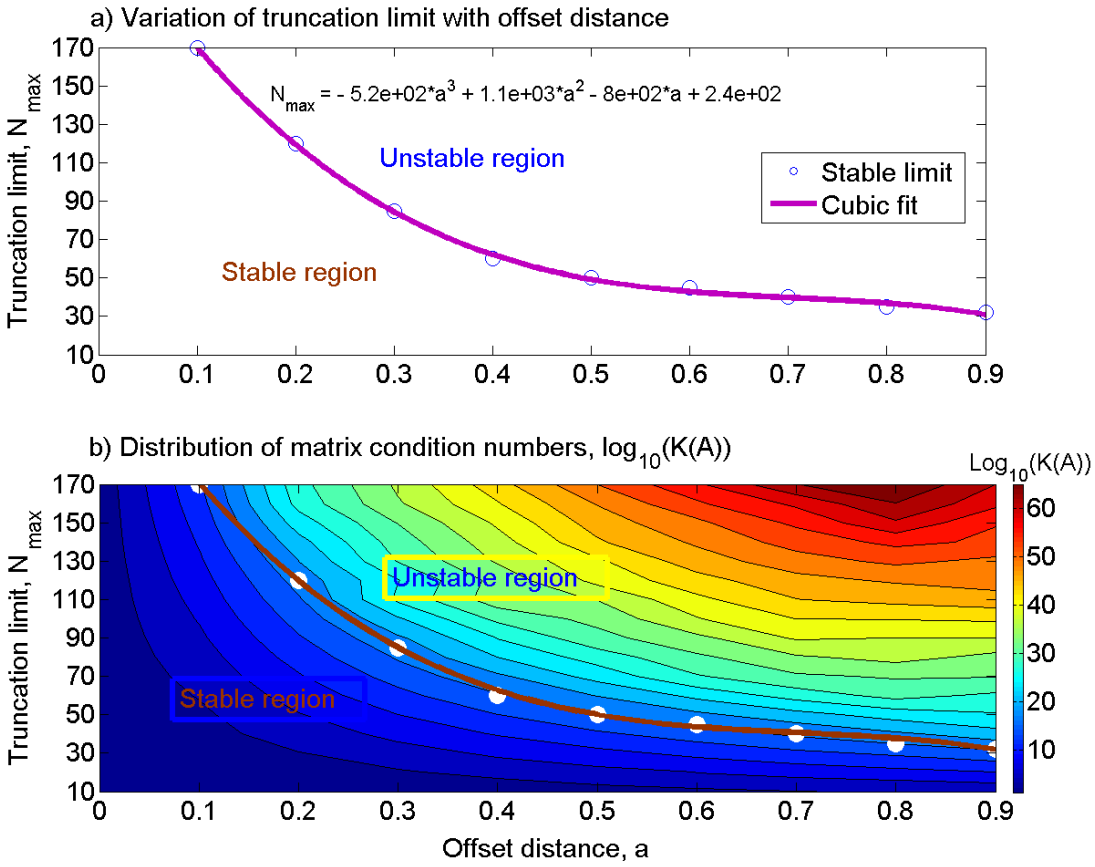

Fig. 3-1 a) Relationship between the optimal number of terms in the general solution required to maintain minimal error in potential field solution and offset distance, b) distribution of condition numbers of coefficient matrix for different offset positions and truncation limits.

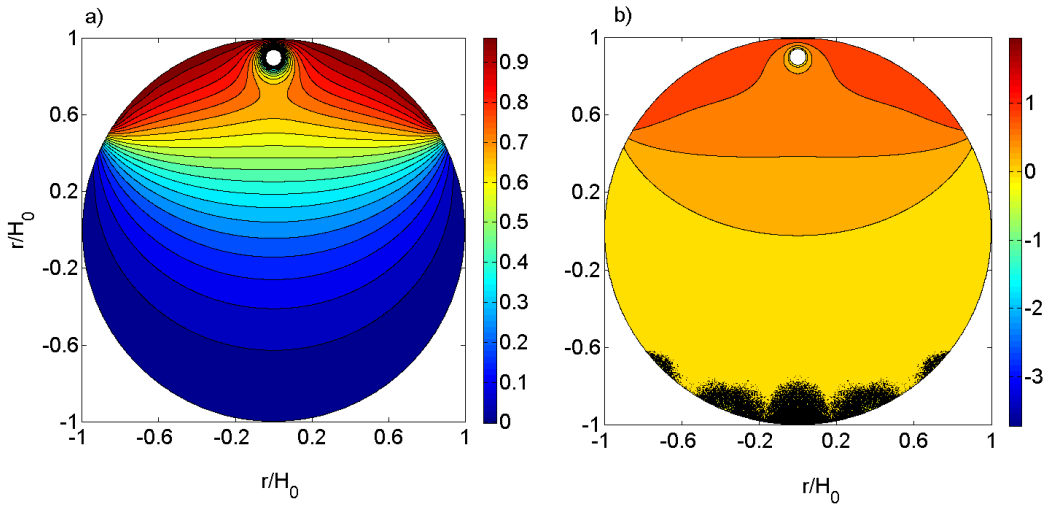

Fig. 3-2 Distribution of normalized potential field solution around a grounded body at offset position, a = 0.9, a) truncation limit, N_{max} = 32, b) N_{max} = 40, effect of truncation error on quality of potential field solution is evident.

The distribution of eigenvalues of a matrix on the complex plane, known as spectra, can provide insight on matrix conditioning and possibility of numerical instability. The spectral radius, $\rho(A)$ of the coefficient matrix defined as the radial extent of the spectrum of the matrix, is used to infer the effect of outlying eigenvalues on quality of the potential field solution using numerical experiments that involve varying ranges of the offset distance and truncation limit. The spectral radius of the coefficient matrix was computed using the Eigtool (Wright, 2002). The coefficient matrices defined by offset distances in the range $a < 0.5$ show no or minimal change in spectral radii with increase in truncation limit and are not shown here. However, the coefficient matrices associated with offset distances in the range $a \geq 0.5$ show moderately large growth in spectral radii with increase in truncation limit (Table 3-1). The large increase in spectral radii,

especially for the offset distance, $a = 0.9$ can be attributed to the presence of outlying eigenvalues which stretch the spectra of the coefficient matrix, leading to increased tendency towards ill-conditioning which can degrade the accuracy of the potential field solution and trigger numerical instability in the solution as discussed earlier.

Table 3-1 The spectral radii of coefficient matrix corresponding to different offset distances and truncation limits.

Truncation Limit, N_{max}	Spectral radii, $Log_{10}\rho(A)$		
	Offset distance, a = 0.5	Offset distance, a = 0.7	Offset distance, a = 0.9
10	0.28	0.28	0.35
20	0.28	0.45	1.06
40	0.36	1.46	2.81
80	1.46	4.21	7.29
160	6.24	14.64	21.48

Effect of Gibbs Phenomenon on Accuracy of Potential Field

Gibbs phenomenon describes the oscillatory behavior of the potential field solution at the surface of the outer circle. This phenomena is observed when a discontinuous function is represented using a continuous function such as Legendre polynomials (Hewitt and Hewitt, 1979). The solution at the surface of the outer circle

oscillates and overshoots values prescribed at the boundary. It is desirable from both a theoretical and practical viewpoint to reduce the oscillatory behavior of the solution at the outer boundary. This problem can be addressed by using a high truncation limit in order to reduce the amplitude of oscillation and ensure convergence to prescribed boundary conditions. However, the truncation limit cannot be increased indefinitely without causing numerical instability in solution, as shown earlier. Therefore, an alternative approach based on the concept of a filter function is employed to reduce the oscillatory behavior of the solution at the boundary of outer circle. The boundary conditions are prescribed using a modified filter function of the form in Roberts and Roberts, (1978) utilized for different application. Fig. 3-3 illustrates the effect of using the modified filter function to prescribe boundary conditions, on oscillatory behavior of potential field solution at the boundary of outer circle. In the case where no filter function is used, the solution overly oscillates about the boundary (Fig. 3-3a). Evidently, the filter function ensures that the oscillations at the boundary are damped out (Fig. 3-3b). It is apparent that the error in the potential field solution is greater when no filter function is used to prescribe boundary conditions, therefore, the filter ensures that the error in the potential field solution at the boundary is bounded.

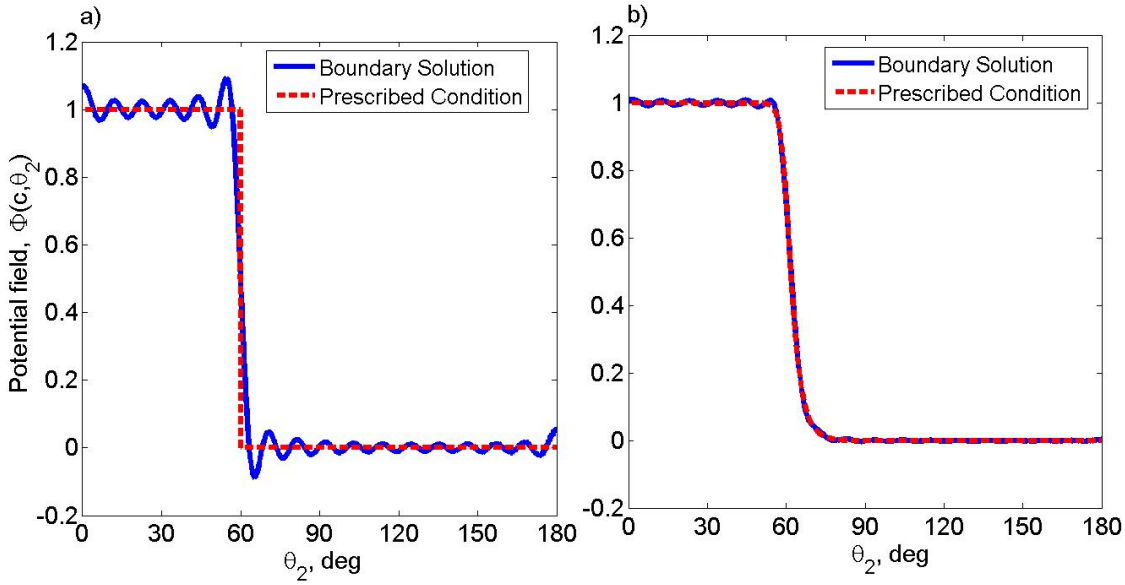

Fig. 3-3 Normalized potential field solution at surface of outer circle, offset position, a = 0.9 and truncation limit, N_{max} = 32, a) boundary conditions prescribed without filter function, b) conditions prescribed using filter function.

Model Validation

The potential field functions developed in this study are validated using closed form solutions to the Poisson problem provided in Reese (1971), Lai et al., (2002), and Lai and Tseng (2007). In all cases, the problem domain is the region contained between two concentric circles and the range of coordinate parameters are $r=[b,c]$, $\theta=[0,\pi]$,where b is the radius of inner circle and c is the radius of outer circle. The validation process involved computing the total potential field solution for three test cases presented in Table 3-2 using the two methods of computing the potential field described previously, i.e. the first method is based on an eigenfunction expansion of Legendre polynomials and spherical Bessel functions while the second approach involves an expansion of Green's

functions and Legendre polynomials. In each test case, the appropriate boundary conditions and forcing function were used for computing the total potential field (Table 3-2). A grid size of $[r,\theta] =$ 1000 x 1441 was used in all test cases, and the angular grid in test case 3 was adjusted slightly by moving the grid points away from the poles in order to avoid singularities in the forcing function. The corresponding total potential field solution in each test case was then compared with the appropriate exact potential field solution and the relative error in each case was computed using the expression of the form, $E = |\Phi(r,\theta) - \Phi_{ex}(r,\theta)|$, where E is the relative error in the total potential field solution, $\Phi(r,\theta)$ is the total potential field solution and $\Phi_{ex}(r,\theta)$ is the exact potential field solution. The exact solutions to the test cases used in the model validation exercise are shown in Fig. 3-4. Further, the effect of truncation limit and diameter of inner circle on size of relative error in the total potential field solution was investigated.

Table 3-2 Test cases used in validation of the Poisson problem in a circular domain.

Test case	1	2	3
Exact solution	$\Phi(r,\theta) = r^3\cos\theta$	$\Phi(r,\theta) = r^4\cos\theta - r^5\cos^2\theta$	$\Phi(r,\theta) = r^3\sin\theta - r^4\sin\theta\cos\theta$
Forcing function	$f(r,\theta) = 10r\cos\theta$	$f(r,\theta) = 18r^2\cos\theta - r^3\left(2+24\cos^2\theta\right)$	$f(r,\theta) = r\left(11\sin\theta+\cot\theta\cos\theta\right) - r^2\left(8\sin 2\theta+\cot\theta\cos 2\theta\right)$
Boundary conditions	$\Phi(b,\theta) = b^3\cos\theta$ $\Phi(c,\theta) = c^3\cos\theta$	$\Phi(b,\theta) = b^4\cos\theta - b^5\cos^2\theta$ $\Phi(c,\theta) = c^4\cos\theta - c^5\cos^2\theta$	$\Phi(b,\theta) = b^3\sin\theta - b^4\sin\theta\cos\theta$ $\Phi(c,\theta) = c^3\sin\theta - c^4\sin\theta\cos\theta$

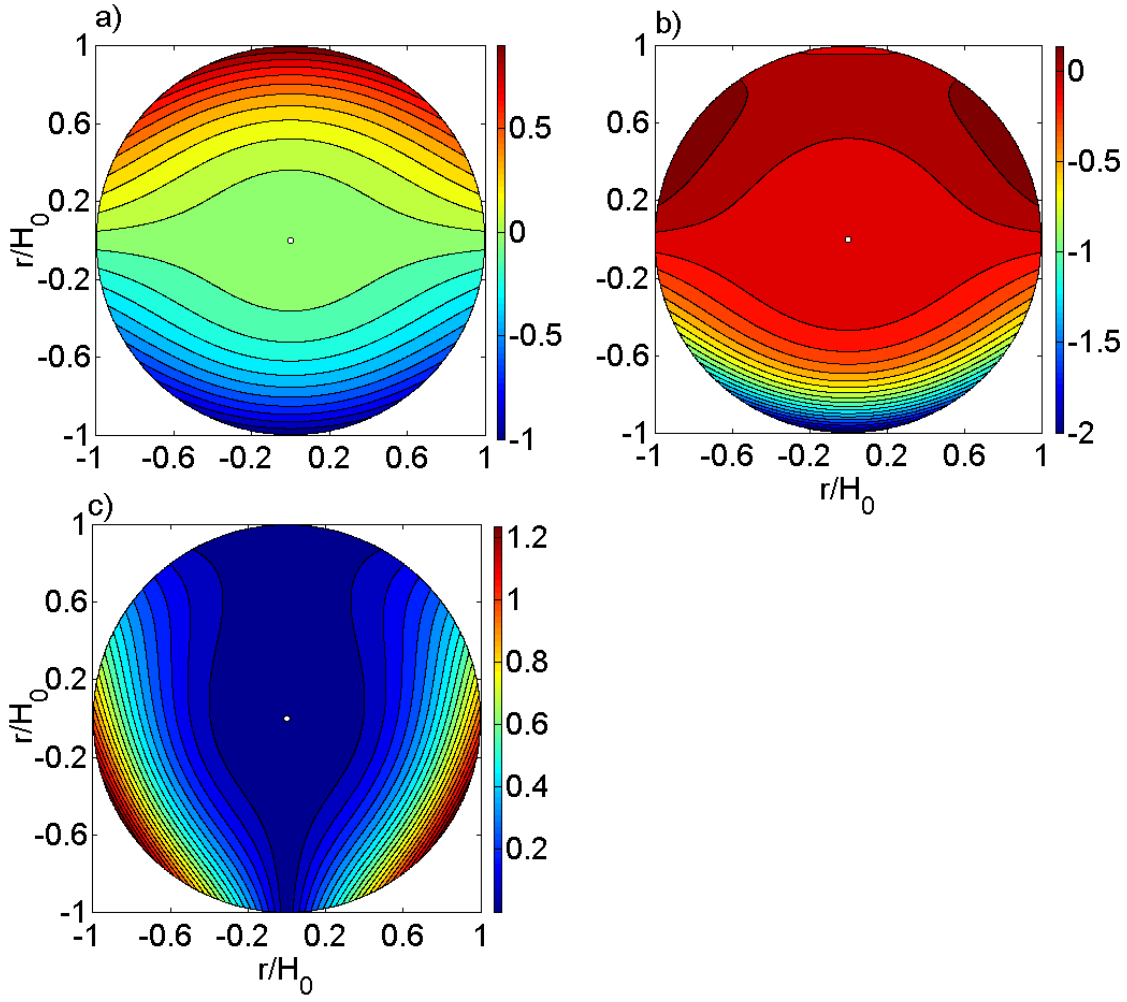

Fig. 3-4 The exact potential field solution for a) test case 1, b) test case 2, and c) test case 3. The diameter of inner circle, $D = 0.03$, was used in all test cases.

Fig. 3-5 through Fig. 3-7 compare the magnitude of the relative error in the total potential field involving both the Bessel functions and Green's function, for test cases 1, 2 and 3 respectively. Generally, the magnitude of the relative error in the total potential field, for test cases 1 and 2, was lower for the solution involving Green's function.

However, for test case 3, the magnitude of the error in the potential function computed using the two methods was comparable, with the total potential field based on Green's function showing slightly lower error. Further, investigation of the effect of truncation limit on size of relative error in total potential field for each test case showed that truncation limits, $J_{\max}$ and $N_{\max}$ for the potential field involving Bessel functions and $N_{\max}$ for solution based on Green's function, depends on the type of the test case.

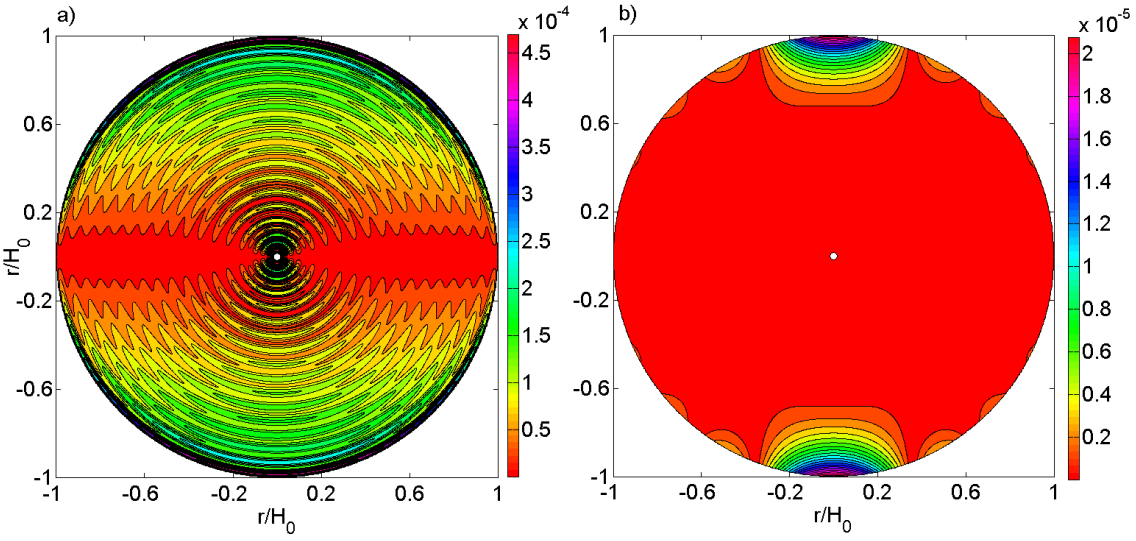

Fig. 3-5 Relative error in total potential field for test case 1, a) solution involves spherical Bessel functions, b) solution involves Green's function. The diameter of the inner circle, D = 0.03.

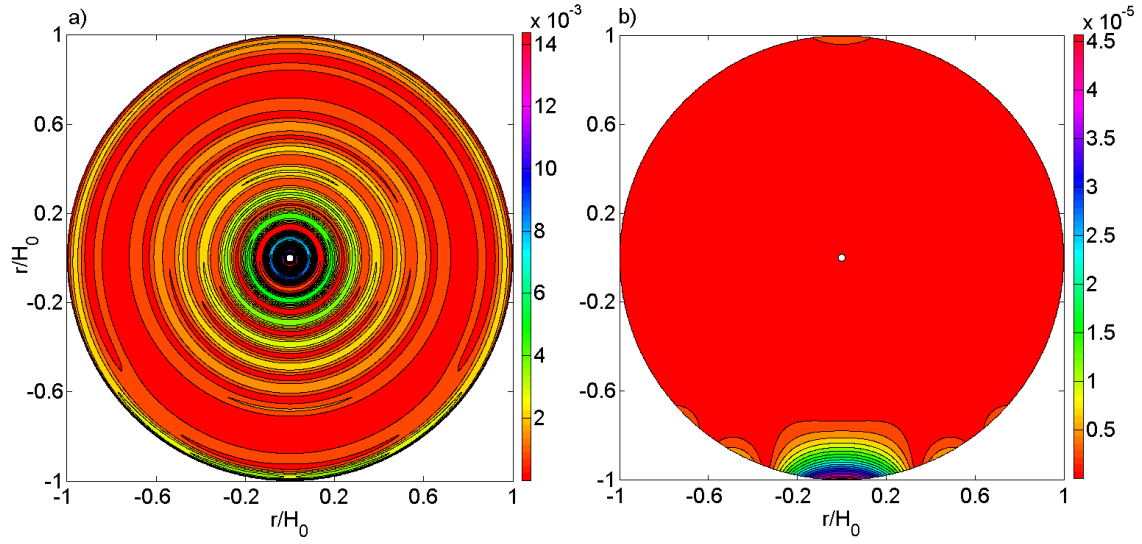

Fig. 3-6 Relative error in total potential field for test case 2, a) solution involves spherical Bessel functions, b) solution involves Green's function. The diameter of the inner circle, D = 0.03.

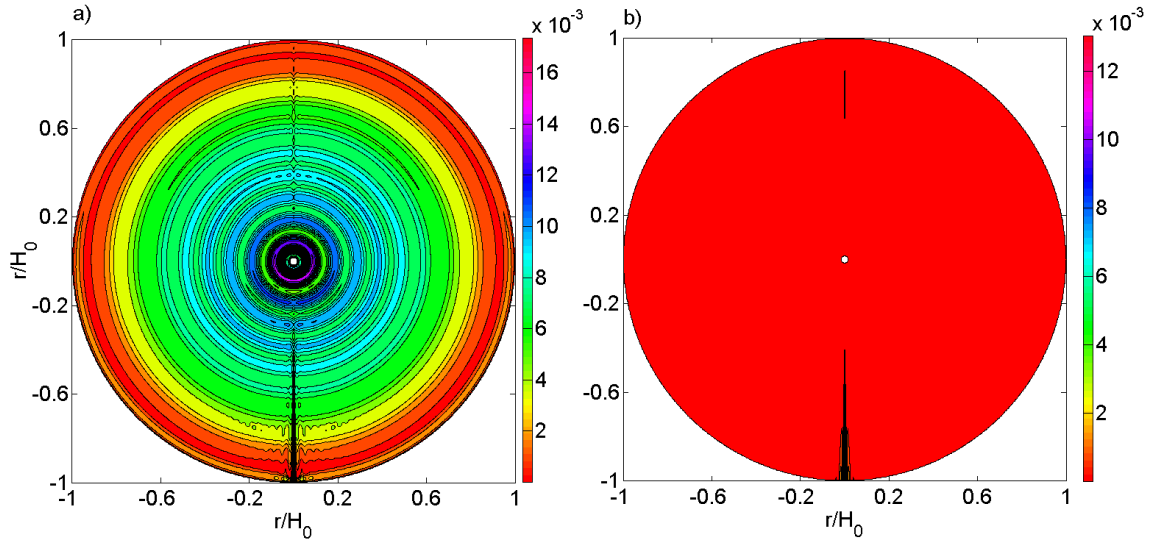

Fig. 3-7 Relative error in total potential field for test case 3, a) solution involves spherical Bessel functions, b) solution involves Green's function. The diameter of the inner circle, D = 0.03.

Considering both methods of computing the total potential field, test cases 1 and 2 required fewer terms in the general solution to resolve the potential field with minimal error. Table 3-3 demonstrates the impact of truncation limit on the maximum relative error in the potential field for the three test cases. For test cases 1 and 2, the relative error in the potential field either increased or stayed constant with increase in truncation limit beyond the optimal. The total potential field in test case 3 computed using both methods, was difficult to resolve and error in the solution decreased slowly with increase in truncation limit. Even with a large number of terms, the size of the error in the solution was still appreciable, because the potential field in this case has a funnel-like structure in the region close to the south-pole and is difficult to resolve with a high degree of accuracy. It is worth noting that, the error analysis for the total potential field involving the Bessel functions in test case 1 was conducted at the optimal truncation limit, $N_{\max} = 10$, since increasing the number of terms, n in the solution beyond this optimal while keeping the $J_{\max}$ truncation limit fixed resulted in either no change or large error in the total potential field.

Further, the relative error in the potential field solution involving Bessel functions showed a dependency on geometry of the problem domain, and increased with diameter of the inner circle as shown in Table 3-4. This phenomena was observed in all test cases and may be attributed to the weighting of the modal coefficients in the general solution which is based on the radius of the inner circle. In addition, the size of error in the potential field was greatest at the boundaries of the inner and outer circles. In contrast, the error in the total potential solution involving Green's function was independent of the diameter of

the inner circle and the largest error in the potential field occurs in the region close to the outer boundary for all test cases considered.

Table 3-3 Maximum relative error, $\max|E|$, in total potential field solution involving Green's function, for the different test cases, diameter of inner circle, $D = 0.03$, for a range of truncation limits.

Truncation limit N_{max}	Test case 1 $\max\|E\|$	Test case 2 $\max\|E\|$	Test case 3 $\max\|E\|$
10	2.18×10^{-5}	4.80×10^{-5}	1.84×10^{-1}
20	8.33×10^{-5}	1.75×10^{-4}	9.55×10^{-2}
40	3.25×10^{-4}	6.67×10^{-4}	4.88×10^{-2}
60	7.26×10^{-4}	1.50×10^{-3}	3.28×10^{-2}
80	1.30×10^{-3}	2.60×10^{-3}	2.47×10^{-2}
100	2.00×10^{-3}	4.00×10^{-3}	1.98×10^{-2}
120	2.90×10^{-3}	5.80×10^{-3}	1.65×10^{-2}

Table 3-4 Maximum relative error, $\max|E|$, in total potential field solution involving Bessel functions, for test case 1, truncation limit, $N_{max} = 10$, for different diameters of the inner circle.

Truncation limit J_{max}	D = 0.03, $\max\|E\|$	D = 0.06, $\max\|E\|$	D = 0.09, $\max\|E\|$
10	3.60×10^{-3}	3.70×10^{-3}	4.80×10^{-3}
20	9.53×10^{-4}	3.50×10^{-3}	2.87×10^{-1}
30	4.94×10^{-4}	3.45×10^{-2}	2.87×10^{-1}
40	5.92×10^{-4}	3.48×10^{-2}	2.90×10^{-1}
50	2.52×10^{-2}	3.48×10^{-2}	2.90×10^{-1}
60	2.50×10^{-2}	3.54×10^{-2}	2.90×10^{-1}

4. LIGHTNING STRUCTURE INTERACTION

Numerical Examples

In this section numerical examples address the effect of elevation, body geometry, cloud and leader parameters on the distribution of total potential field. Consequently, the total potential field provides a basis for evaluating regions of high risk, electrical surface charge and lightning collection area around the grounded structure as a function of the offset position, a , diameter of airborne structure, D , angular extent of cloud cover, ϑ and downward leader angle, θ_0. The offset position defines the distance between the centers of the inner and outer circle, and is used here as a measure of the elevation of the structure above the ground surface. Further, the electrical charge and specific energy dissipated during a lightning strike to a grounded structure was computed as a function of the leader peak current.

Parameters for Numerical Simulation

The range of key parameters selected for this research study reflect typical values reported in literature (Miyake, 1990; Rakov and Uman, 2003; Roberts et al., 2007). The range of the parameters are, dimensionless offset position, $a =$ -0.75, -0.5,-0.25, 0, 0.5; the dimensionless diameter of structure, $D =$ 0.03, 0.06, 0.09 and 0.12; extent of cloud cover, $\vartheta =$ 0-60, 0-75 and 0-90 degrees and downward leader angle, $\theta_0 =$ 0 and 45 degrees. The elevation of the cloud, H_0, was taken as 4000 m. A leader peak current of 20 kilo-amperes and potential gradient at the base of the cloud of 40 kilo-volts/m were

used in calculations involving regions of high risk around airborne structures. For calculations involving surface charge density, a leader peak current of 20 kilo-amperes, dimensionless leader length of $0.75-a$ and potential gradient at the base of the thundercloud of 100 kilo-volts/m were considered. A range of leader peak currents of 10 to 105 kilo-amperes were used in calculations involving electrical charge and specific energy dissipated during a lightning strike to a grounded structure. The range of leader peak currents of 20 to 100 kilo-amperes and potential gradient at the base of thundercloud of 100 kilo-volts/m were used for evaluating lightning collection area.

Modeling Potential Field and Regions of High Risk

Numerical experiments were conducted to explore the sensitivity of the total potential field and regions of high risk to changes in the key parameters. In the first experiment, the offset position, diameter of the airborne structure and size of cloud cover were varied while the downward leader angle was kept constant. In the second experiment, the downward leader angle was varied while the offset position, cloud cover and diameter of the structure were kept constant. In all cases, the normal joint probability density function of the upward leader lengths and the angle on the surface of the structure was computed. Further, the probability of a lightning strike attaching to the airborne structure was computed as the mean of the ratio of the length of the upward leaders, incepted from the surface of the structure, and the length of the longest upward leader in the entire set of simulations. The resulting value is then multiplied by a normalized fraction of the region of high risk on the airborne structure.

Potential Field around Airborne Structure

The accuracy of the total potential field around an elevated grounded structure computed using the two different methods discussed previously was investigated. Generally, the potential field involving spherical Bessel functions shows increased spreading and is accurate in cases where the downward leader is distant from the structure. The spherical wave functions cannot adequately capture the radial distribution of the potential field induced by the downward leader, especially when the leader is very close to the structure. However, the potential field is accurate for practical applications in cases where the tip of the downward leader is far from the structure. In contrast, the field involving the Green's function is concentrated about the axis of the downward leader and since, the integration limits in the general solution involving the Green's function are inherently linked to the boundary conditions, the potential field is accurate when the downward leader tip is close to the structure. Typically, regions of high risk are computed when the downward leader is distant from the structure, therefore the total potential field involving the spherical Bessel functions is used for determining probable points of lightning attachment on the structure.

Effect of Elevation and Size of Airborne Structure

The behavior of the total potential field around an airborne structure was investigated as a function of elevation and diameter of the elevated structure. The distribution of the total potential field around the airborne structure changes with elevation as illustrated in Fig. 4-1. The potential field around the airborne structure is highest when the elevated body is positioned closest to the thundercloud, and the field decreases in

magnitude as the elevated structure moves towards to the ground surface. Further, the distribution of the potential field in the immediate vicinity of the airborne structure changes with diameter as illustrated in Fig. 4-2. It is evident that increasing the size of the airborne structure decreases the magnitude of the potential field around the body. Since the structure is assumed to be perfectly conducting, the ambient potential field around the airborne structure is highly perturbed and the response is magnified with increase in size of the elevated structure.

The corresponding distribution of upward leaders incepted from the surface of the structure for different diameters, and varying elevations above the ground surface was studied. For this particular case, the downward leader is assumed to propagate along the vertical axis. It is evident that the joint probability density function of the upward leaders incepted and angle on the surface of the airborne structure is symmetrical about the angle of the downward leader and the magnitude of the incepted upward leaders decrease as the structure moves closer to the ground surface as illustrated in Fig. 4-3. Again, this behavior is consistent with the distribution of the total potential field around the airborne structure.

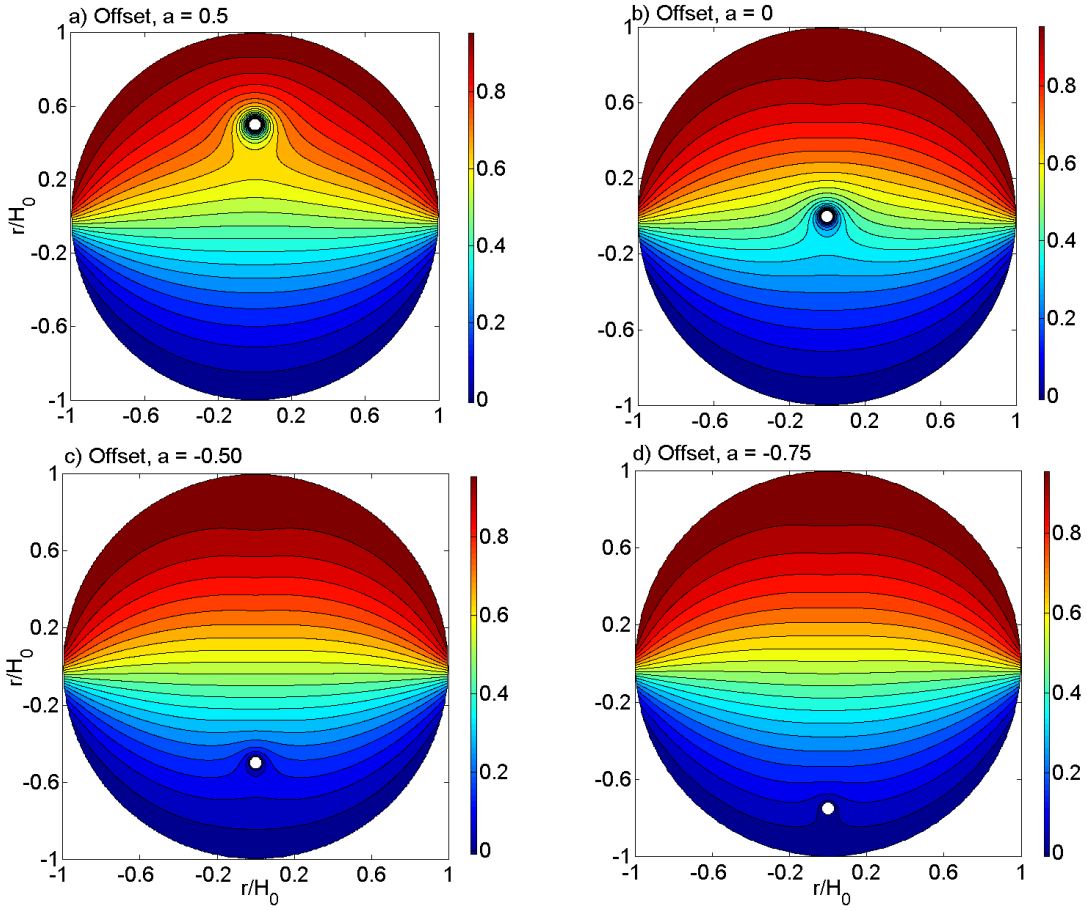

Fig. 4-1 Distribution of normalized total potential field around a grounded structure of diameter, $D = 0.06$, for offset position, a) $a = 0.5$, b) $a = 0$, c) $a = -0.5$ and d) $a = -0.75$. The length of downward leader is $L_D = 0.25$ for the body at offset position, $a = 0.5$ and $L_D = 0.75$ for the remaining test cases.

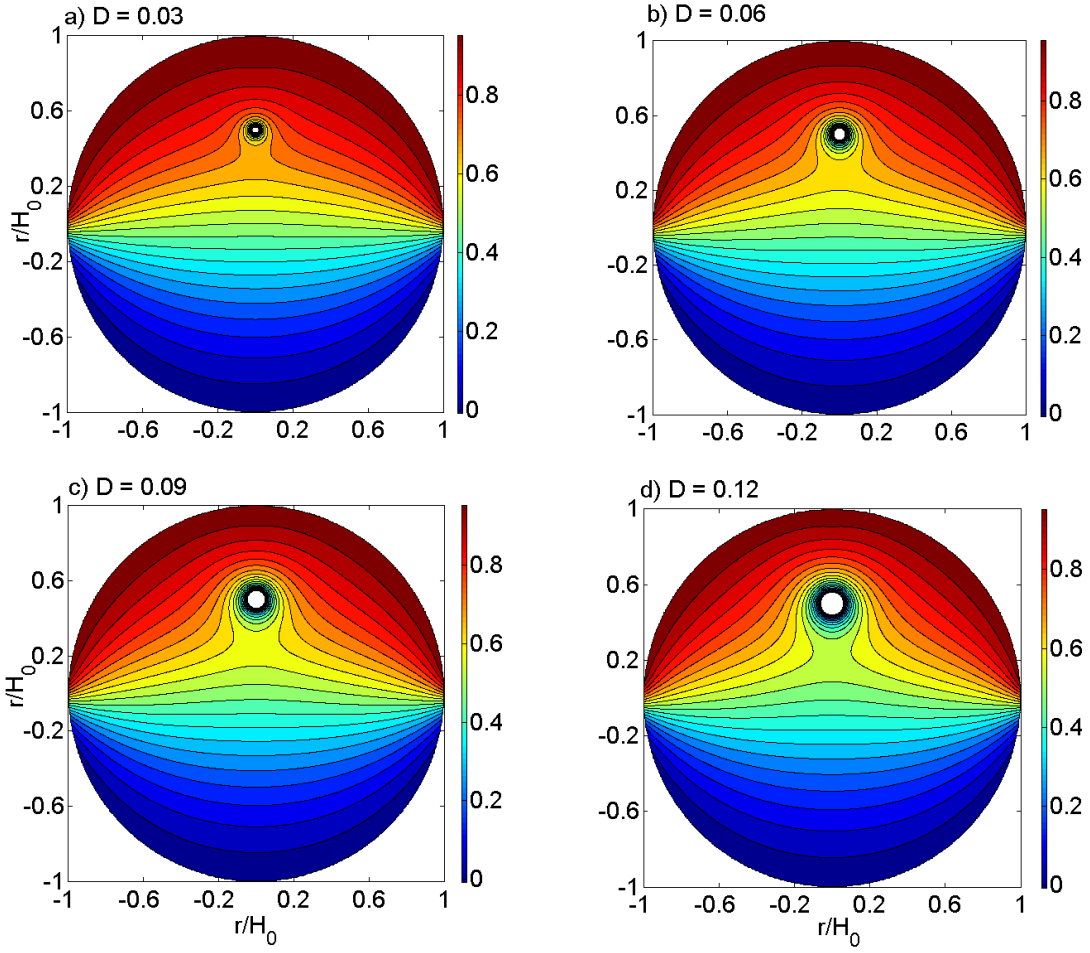

Fig. 4-2 Distribution of normalized total potential field around a grounded body of diameter, a) $D = 0.03$, b) $D = 0.06$, c) $D = 0.09$ and d) $D = 0.12$. The offset position, $a = 0.5$ and the length of downward leader, $L_D = 0.25$ were used in all test cases. The potential field induced by downward leader is computed using Bessel functions.

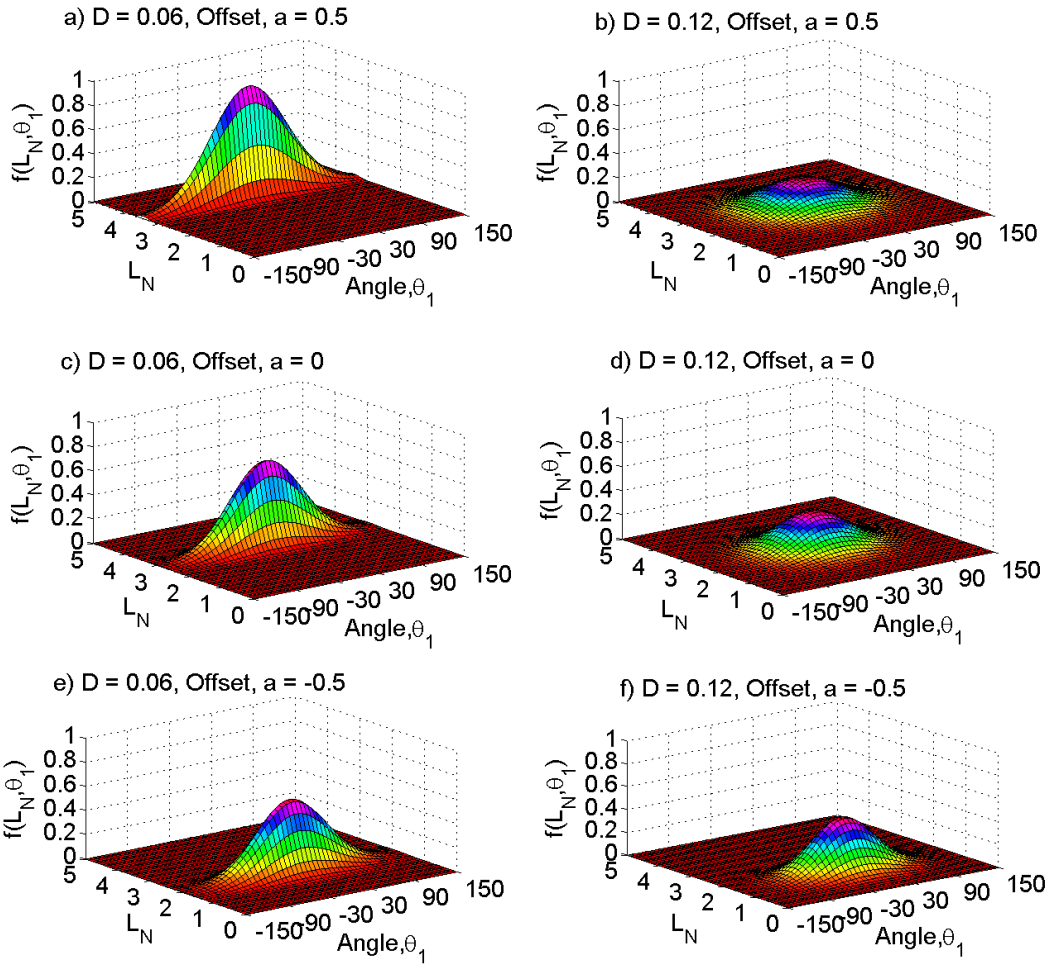

Fig. 4-3 Plots of normalized joint probability density function, $f(L_N,\theta_1)$ of upward leader lengths and the angle on the surface a grounded structure for a) $D = 0.06$, $a = 0.5$, b) $D = 0.12$, $a = 0.5$, c) $D = 0.06$, $a = 0$, d) $D = 0.12$, $a = 0$, e) $D = 0.06$, $a = -0.5$ and f) $D = 0.12$, $a = -0.5$. The extent of cloud cover, $\vartheta = 0$-90 deg., downward leader angle, $\theta_0 = 0$ deg., and L_N is the logarithm of the length of the upward leader.

Since the magnitude of the incepted upward leaders is related to the strength of the potential field around the body, the curves show a downward shift as the structure moves away from the region of high potential field, typical located close to the thundercloud. The joint probability density functions computed are sensitive to the range of upward leader lengths, and thus the probability curves are narrow for the case where the leader lengths have a short range, and broad where the range of the leader lengths is large.

Further, the probability of lightning attaching on the structure, $P(s)$ was shown to increase with the elevation of the structure above the ground surface, and decrease with increase in size of the structure as demonstrated in Table 4-1. Increasing the peak current in the lightning strike increases the magnitude of the incepted upward leaders but the trends discussed above are unchanged. Similar trends in upward leader curves are observed in the case of upward triggered lightning from the grounded structure in absence of a distinct downward leader. In this case, upward leaders are triggered from the surface of the elevated structure when the background potential field exceeds the threshold for upward leader inception.

Table 4-1 Summary of the probability of lightning attachment, $P(s)$ on a grounded structure deployed at different elevations above the ground surface for varying cloud coverage and diameter of structure, and the angle of downward leader, $\theta_0 = 0$ deg.

a	$P(s)$ $\vartheta =$ 0-60 deg.			$P(s)$ $\vartheta =$ 0-75 deg.			$P(s)$ $\vartheta =$ 0-90 deg.		
	$D =$ 0.03	$D =$ 0.06	$D =$ 0.12	$D =$ 0.03	$D =$ 0.06	$D =$ 0.12	$D =$ 0.03	$D =$ 0.06	$D =$ 0.12
0.5	0.2288	0.1045	0.0248	0.3376	0.1590	0.0358	0.4326	0.2094	0.0440
0	0.0276	0.0117	0.0049	0.0666	0.0290	0.0116	0.1346	0.0601	0.0224
-0.5	0.0024	0.0011	0.0005	0.0061	0.0027	0.0012	0.0147	0.0066	0.0031

Effect of Extent of Cloud Cover

The effect of the extent of cloud cover on the distribution of the total potential field around a grounded body and the corresponding distribution of upward leaders incepted from the surface of the body was studied. The total potential field around the elevated grounded body shows distinct changes with variation in size of cloud clover as illustrated in Fig. 4-4. The region of high potential field is larger for the cloud cover of the widest extent while that of the cloud of the smallest coverage was limited in spatial extent. On closer observation, the probability distribution of the potential field in the immediate vicinity of the structure changes with the size of cloud cover as illustrated in Fig. 4-5. These changes in potential field can be attributed to large spreading of the field associated with increase in cloud cover size. Consequently, the probability of lightning attachment on the grounded structure increases with size of cloud cover (Table 4-1). Again, these trends are consistent with the distribution of the total potential field around the grounded structure, with clouds of a larger extent inducing high potential fields required to incept upward leaders which propagate longer distances, increasing the probability of attachment with the downward leader.

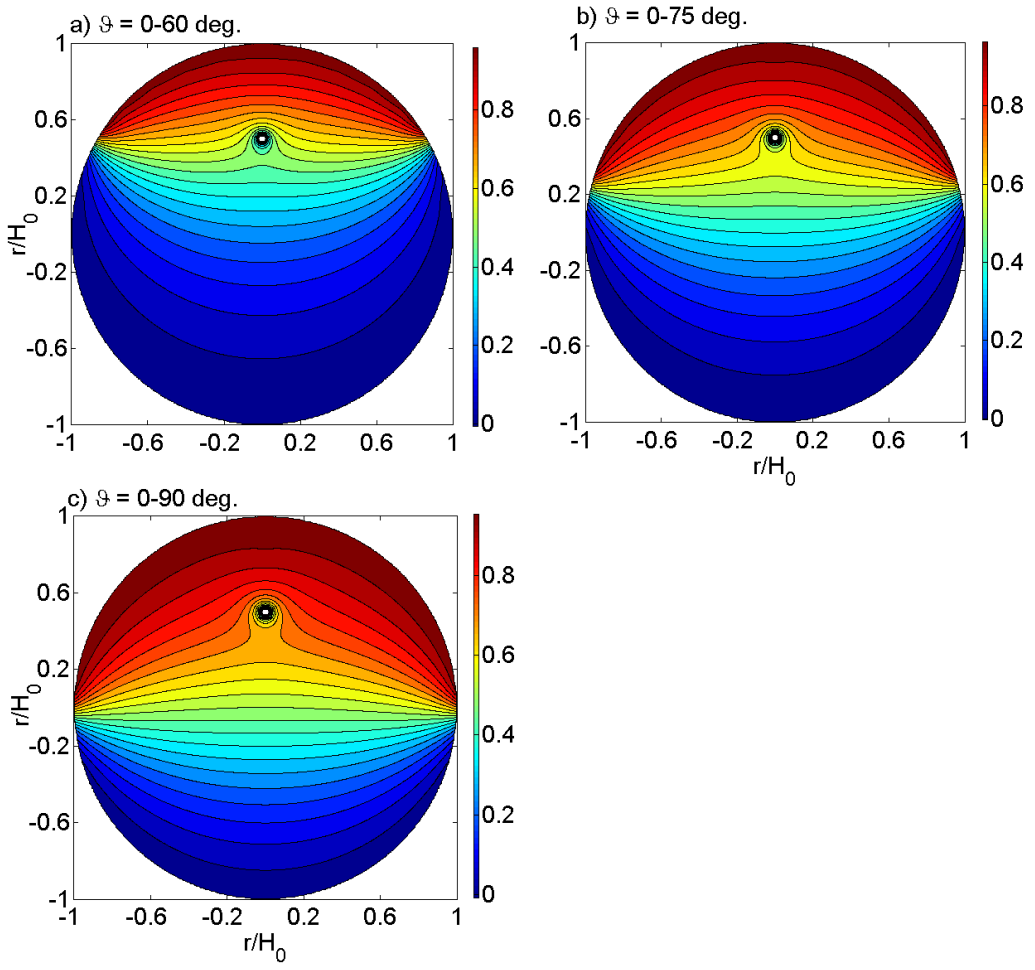

Fig. 4-4 Distribution of normalized total potential field around a grounded body of diameter, $D = 0.03$ at offset distance, $a = 0.5$, for cloud cover extent of, a) $\vartheta =$ 0-60 deg., b) $\vartheta =$ 0-75 deg., and c) $\vartheta =$ 0-90 deg. The downward leader length, $L_D = 0.25$ and angle of the leader, $\theta_0 =$ 0 deg., was used in all test cases.

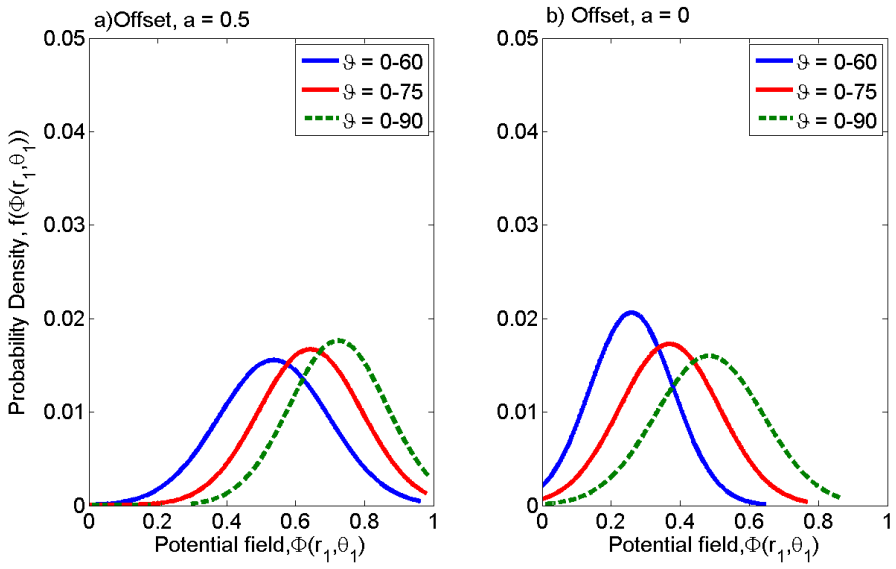

Fig. 4-5 Probability density function of the normalized total potential field around a radial band of 0.4 from surface of a grounded body of diameter, $D = 0.03$, for cloud cover of different extent for a) offset distance, $a = 0.5$, leader length, $L_D = 0.25$ and b) offset distance, $a = 0$, leader length, $L_D = 0.75$. The angle of the downward leader, $\theta_0 = 0$ deg., was used in all test cases.

Effect of Angle of Downward Leader

The effect of varying the downward leader angle on the behavior of the total potential field and the resulting joint probability density function of the upward leaders incepted and the angle on surface of the structure was investigated. A downward leader propagating from an oblique angle to the body introduces asymmetry in the total potential field which in turn affects the spatial distribution of regions of high risk on the structure as illustrated by the joint probability density functions in Fig. 4-6. The rotation in the joint probability curve corresponding to the oblique downward leader angle is attributed to the asymmetry in the potential field caused by the downward leader. The peak of the upward

leader curves remains relatively unchanged with variation in the downward leader angle, however, the position of the peak and angular extent of the curves shift towards the angle of the downward leader. In this case, the region of high risk on the surface of the structure shifts with the position of the downward leader, implying that the largest allowable downward leader angle defines the extreme extent of the region of high risk on the surface of the structure. The corresponding probability of a lightning strike to the structure was shown to decrease with increase in the downward leader angle.

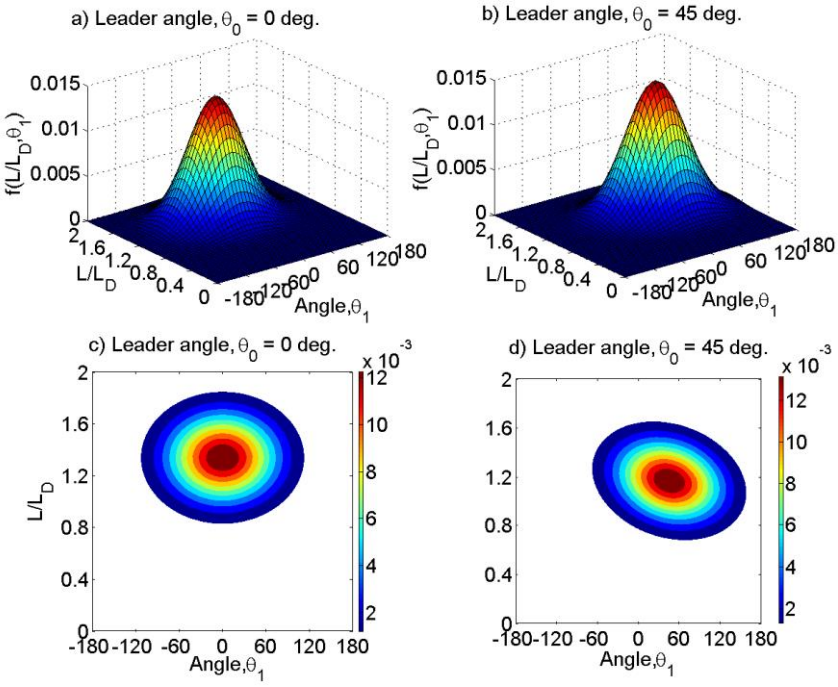

Fig. 4-6 Joint probability density function of upward leader lengths and the angle around the surface of a grounded body of diameter, $D = 0.03$, for the downward leader angle at a) 3D plot, $\theta_0 =$ 0 deg., b) 3D plot, $\theta_0 =$ 45 deg., c) contour plot, $\theta_0 =$ 0 deg., d) contour plot, $\theta_0 =$ 45 deg. The length of the downward leader, $L_D =$ 0.75, offset position, $a =$ 0, cloud cover extent, $\vartheta =$ 0-90 deg., were used in the analysis.

Modeling Surface Electrical Charge on Structures of Different Geometry

The electrical charge induced on the perimeter of an airborne structure was investigated as a function of body shape and elevation. The body shapes and dimensions selected are characteristic of an airborne wind turbine and a heavy lift airship. Three different types of airborne wind turbine each with a different body geometry but similar length were considered. The geometries of the airborne wind turbine are conical cylinder, a two piece cylinder with different diameters and a uniform cylinder, each 30 m long. The conical cylinder is comprised of diameters ranging from 10 m to 20 m while the two piece cylinder is comprised of two uniform cylinders of similar length but different diameters, 10 m and 20 m, respectively. The uniform cylinder has a diameter of 20 m. Five airships of different geometry but similar length were chosen for the analysis. The geometries considered are a uniform cylinder and an elliptic cylinder. Four different uniform cylinders, each 280 m long, with diameters of 20 m, 30 m, 40 m and 60 m, respectively and a single elliptic cylinder, 280 m long, comprised of varied diameters ranging from 10 m to 60 m.

In order to compare the likelihood of lightning attachment on an airborne system, modeled using different body geometries, one type of body configuration must be selected as the reference case. The total surface electrical charge is computed on all airborne structures of different geometry. Then a normalized relative intensification factor is computed that reflects the degree of magnification of the potential gradient on the perimeter of the remaining airborne structures with respect to the values associated with the reference case. For airborne structures of varying diameter, the structure is discretized

into cylindrical elements of different diameter and the surface electrical charge on each element was computed as a function of element diameter and then converted into a function of length as illustrated in an example in Fig. 4-7. It is evident that the surface electrical charge decreases exponentially with diameter and distance along the airborne structure. Consequently, the total surface electrical charge on the airborne structure was computed by integrating the electrical charge function as shown in Equation 39. The number and spacing between cylindrical elements for the conical and two piece cylindrical structures, representing the airborne wind turbine, and the elliptic structure, representing the heavy lift airship, utilized in the calculation of surface electrical charge are shown in Table 4-2. In the case of an airborne structure represented in the form of a uniform cylinder, the surface electrical charge is computed as a function of the diameter and the resulting value is multiplied by the length of the structure to determine the total surface electrical charge.

The impact of elevation and body geometry on surface electrical charge and intensification factor on the three cylindrical structures, representing an airborne wind turbine, are illustrated in Table 4-3. Generally, the magnitude of the total electrical charge on the perimeter of the airborne structure decreases with the elevation of the airborne body. The largest surface electrical charge is on the airborne structure positioned closest to the thundercloud, due to the increase in the electrical potential gradient on the perimeter of the structure with elevation. These trends are consistent with the distribution of the potential field around the structure deployed at different elevations above the ground surface illustrated earlier.

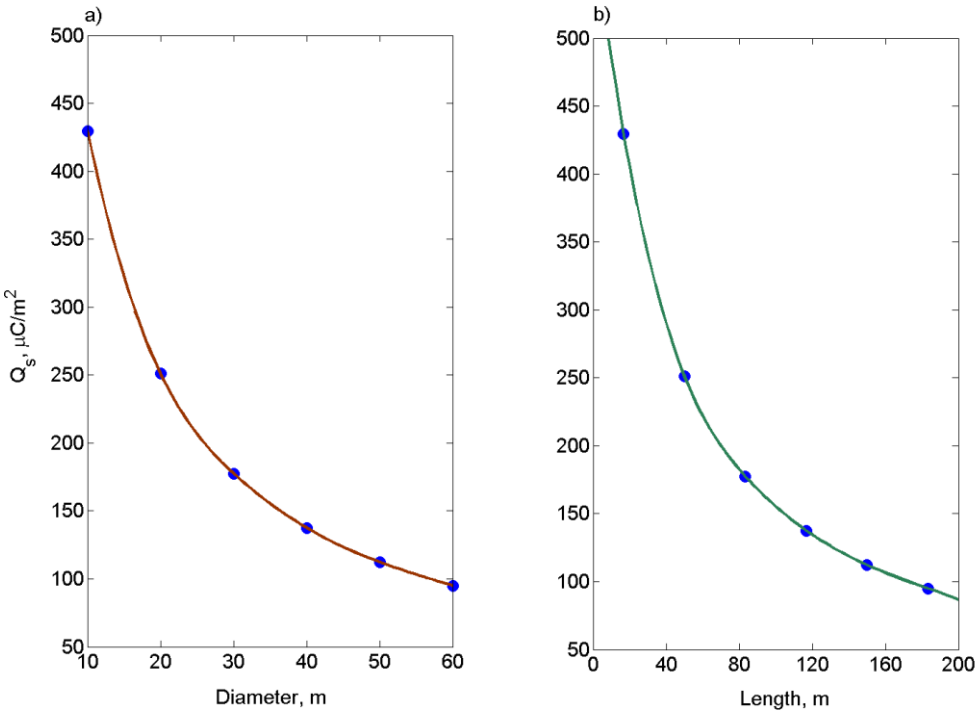

Fig. 4-7 Distribution of electrical charge induced on a section of an elliptic long cylinder as a function of, a) length of structure, D and b) diameter of structure, L.

Table 4-2 Discretization of airborne structures of varied diameter.

Body geometry	Number of elements	Range of element diameter (m)	Spacing between elements (m)	Total length of structure (m)
Conical cylinder	5	10-20	6	30
Two piece cylinder	2	10-20	15	30
Elliptic cylinder	9	10-60	20-34	280

Further, the shape of the airborne structure has an impact on the magnitude of electrical charge induced on the elevated structure. The uniform cylinder has the smallest electrical charge while the two piece cylinder has the largest surface electrical charge. The differences in the magnitude of the surface electrical charge are attributed to the effect of body shape and size in perturbing the ambient potential field, the two piece cylinder has a fairly long slender section which magnifies the potential gradient around that section of the airborne structure leading to a high magnitude of electrical charge. In contrast, the uniform cylinder has a broad shape leading to a uniform moderate potential gradient along the entire structure which yields a lower surface electrical charge. The mean intensification factor was computed by averaging the intensity factors at four different elevations because of the minimal variation in the intensification factor for a given shape with elevation. In the case of the cylindrical structures representing the airborne wind turbine, the uniform cylinder was treated as the reference case. Both the conical cylinder and two piece cylinder show moderately high intensification factors of similar magnitude implying that the potential gradient on these shapes is highly magnified, compared to the base the reference case, and the probability of upward leader inception and lightning attachment is higher compared to the uniform cylinder.

Table 4-3 Surface electrical charge, Q_t induced on cylindrical structures of varied geometry, representing an airborne wind turbine, as a function of elevation.

Shape	$a = 0.5$ $Q_t(\mathrm{m}C/m)$	$a = 0$ $Q_t(\mathrm{m}C/m)$	$a = -0.5$ $Q_t(\mathrm{m}C/m)$	$a = -0.75$ $Q_t(\mathrm{m}C/m)$	$\Delta Q_t(\%)$
Uniform cylinder	7.53	4.88	2.07	1.17	
Conical cylinder	9.89	6.42	2.72	1.54	31.2
Two piece cylinder	10.21	6.63	2.81	1.59	35.4

The impact of elevation and body geometry on the surface electrical charge and the corresponding intensification factors on cylindrical structures representing the heavy lift airship are illustrated in Table 4-4. Again, the surface electrical charge decreases with elevation and the most slender structure positioned closest to the thundercloud has the largest surface electrical charge while the broadest structure deployed close to ground surface has the smallest. The intensification factor was computed in all the cases with the elliptic cylinder treated as the reference case. It is interesting to note that cylindrical structures with diameters in the range of 30 m to 60 m show negative intensification factors, with the highest factor associated with the largest structure. In this case, the negative factors indicate that potential gradient on the surface of the airborne structure under consideration is lower compared to the value on the reference structure suggesting that the probability of leader inception and lightning attachment is reduced compared to the reference case. On the other hand, the most slender cylindrical structure shows a positive intensification factor, implying a high probability of upward leader inception and lightning attachment on the perimeter of the airborne structure compared to the reference case.

Table 4-4 Surface electrical charge on cylindrical structures, representing the heavy lift airship as a function of body geometry and elevation.

Shape	$a = 0.5$ $Q_t(\mathrm{m}C/m)$	$a = 0$ $Q_t(\mathrm{m}C/m)$	$a = -0.5$ $Q_t(\mathrm{m}C/m)$	$a = -0.75$ $Q_t(\mathrm{m}C/m)$	$\Delta Q_t(\%)$
UC, $D = 20$ m	70.30	45.57	19.34	10.96	30.3
UC, $D = 30$ m	49.72	32.20	13.71	7.80	-7.7
UC, $D = 40$ m	38.50	24.92	10.65	6.08	-28.4
UC, $D = 60$ m	26.58	17.19	7.40	4.25	-50.3
Elliptic cylinder	53.87	34.91	14.86	8.44	

Electrical Charge and Specific Energy Dissipated in Lightning Strike

The electric charge dissipated during a lightning strike to a grounded structure was computed as two separate contributions. The first part was charge dissipated during short stroke process and second contribution is charge transferred during the long stroke process. Fig. 4-8a illustrates the shape of the wave form for short stroke electric current while Fig. 4-8 b shows the wave form for the long stroke electric current. The short stroke current appears as short duration impulse while the long stroke current is characterized by a uniformly distributed electric current load that occurs over an extended period of time, typically up to 1.0 s.

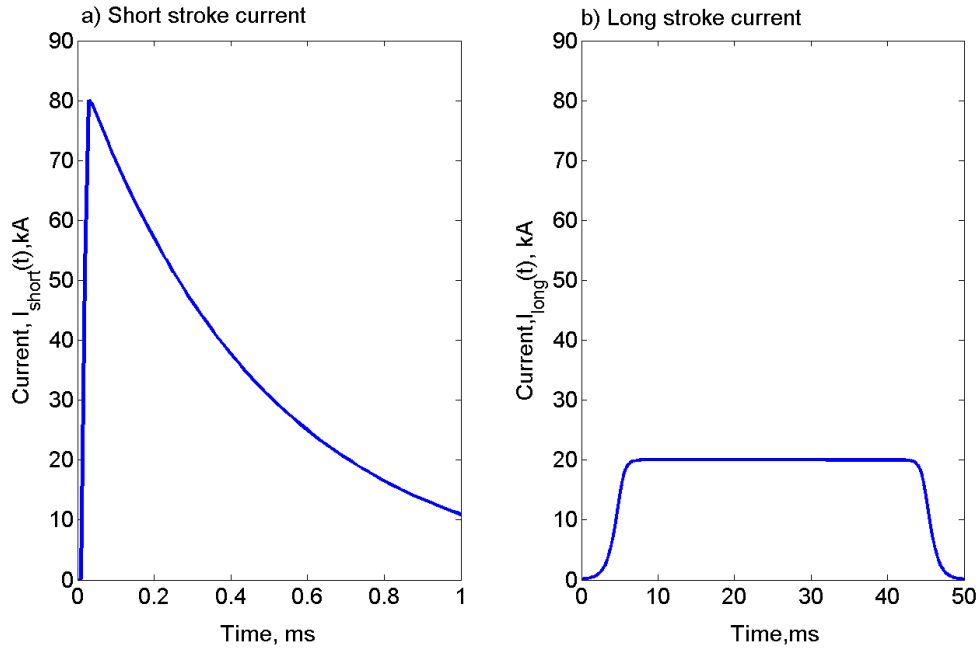

Fig. 4-8 An example of a wave form for, a) short stroke electric current, b) long stroke electric current.

Fig. 4-9 shows the distributions of the peak current and charge dissipated during the short and long processes of a lightning strike to a grounded structure. The charge dissipated was normalized using the length of the grounded structure, here a total length of 60 m was assumed. The charge from the long stroke process makes up the largest contribution of charge dissipated during a lightning strike to a ground structure because of its long duration. Fig. 4-10 illustrates the specific energy dissipated during a lightning strike during the short and long stroke processes. Based on these estimates, the total charge and specific energy exceed the design threshold recommended for sizing lightning protection on grounded structures. This implies that the criteria for designing lightning protection on grounded structures can be inadequate in cases where large impulses of

energy are dissipated through a grounded structure and thus need for improved design criteria maybe warranted in these cases.

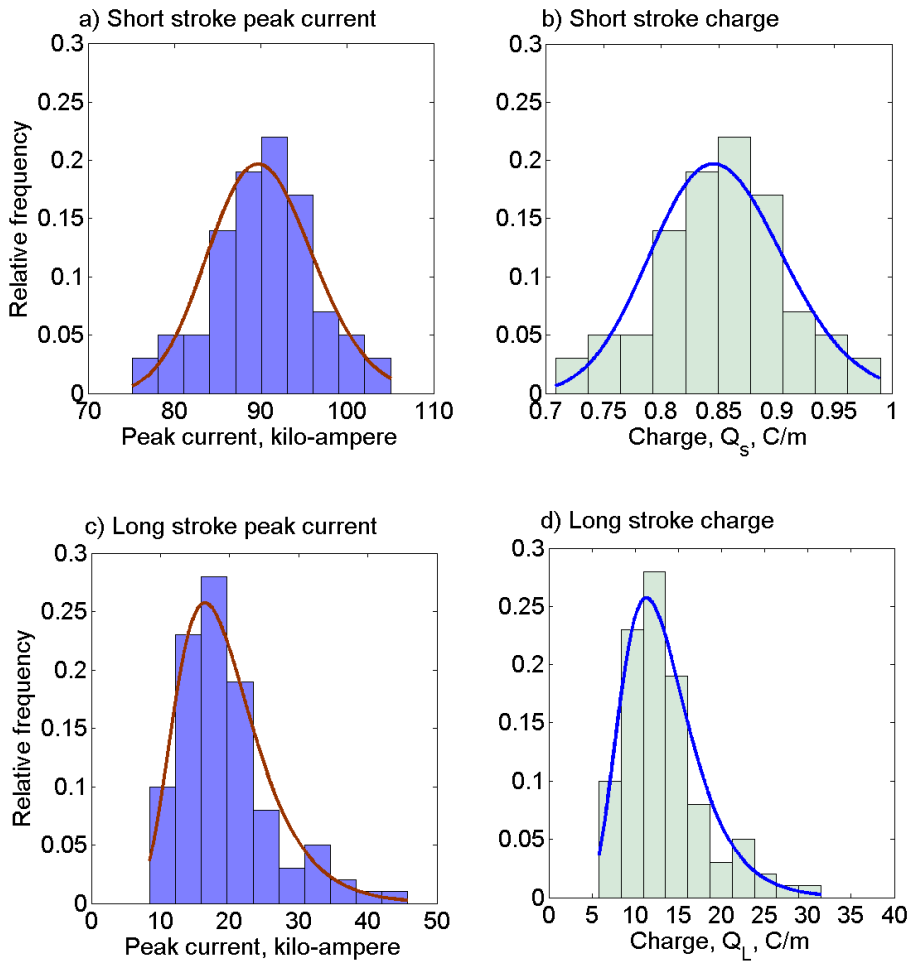

Fig. 4-9 Probability distribution of a) short stroke peak current, b) charge dissipated during short stroke process, Q_s, c) long stroke peak current, d) charge transferred during long stroke process, Q_L. The length of the grounded structure, $L =$ 60 m.

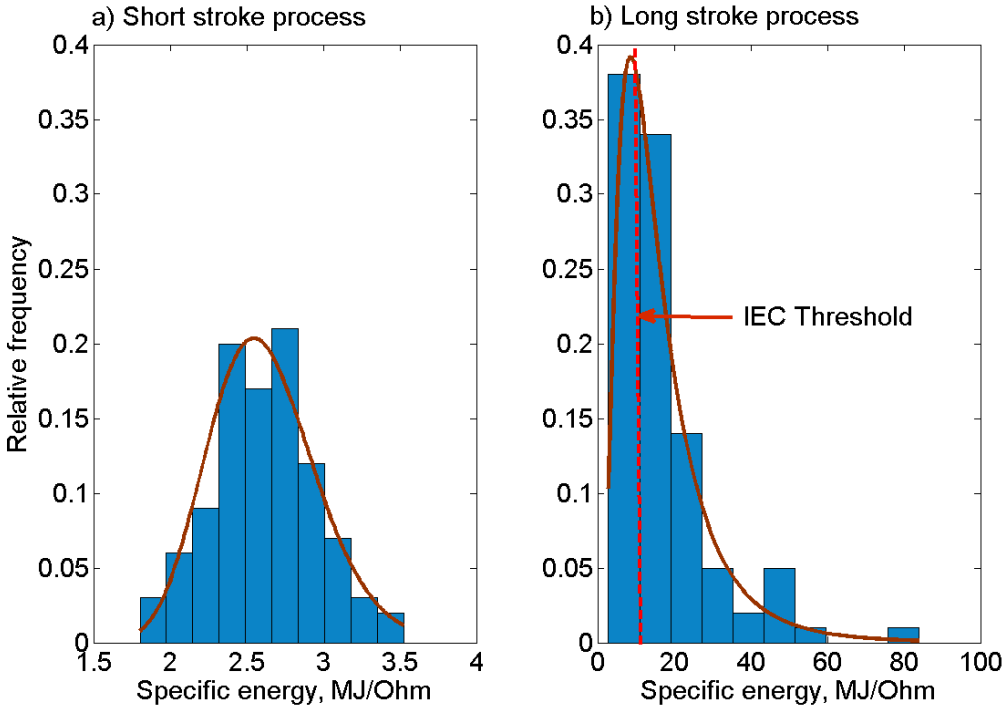

Fig. 4-10 The specific energy contribution from, a) short stroke current, b) long stroke current.

Lightning Collection Area and Strike Frequency

The effect of elevation, diameter of the grounded structure and angle of downward leader on striking distance and the corresponding lightning collection area and strike frequency was investigated. The lighting collection area for a grounded structure positioned at the offset distances, $a =$ 0 and -0.25, is represented using the log-normal probability distribution while the Weibull distribution characterizes lightning collection areas corresponding to the structure deployed at the offset distances, $a \geq -0.5$. The probability functions for both the log-normal and Weibull probability distributions are described in Appendix B.

The normalized lightning collection area for a grounded structure of a smaller diameter, $D = 0.03$, deployed at varying elevations above the ground surface is illustrated in Fig. 4-11. It is evident that the magnitude of the normalized lightning collection area increases with the elevation of the structure above the ground surface, with the structure deployed closest to the ground showing the smallest collection area. This trend can be attributed to the decrease in striking distance as the structure moves away from the region close to the thundercloud where the potential field is greatest. For structures positioned at high elevations, the effect of the potential field from the downward leader is minimal while the potential field contribution from the thundercloud is large and dominant in determining the magnitude of the striking distance. In this case, the relationship between striking distance and the leader peak current is close to linear. In contrast, the potential field contribution from the downward leader is dominant in determining the striking distance for a structure located close to the ground surface and the variation in the striking distance with the leader peak current is non-linear. It is worth noting that the striking distance around a grounded structure deployed at very high elevations, i.e. the offset position, $a > 0$, depends on the distance between the base of the thundercloud and the structure since the threshold for the mean potential gradient associated with the striking distance is exceeded. For such a case, downward lightning is either very minimal or probably non-existent and upward triggered lightning is predominant.

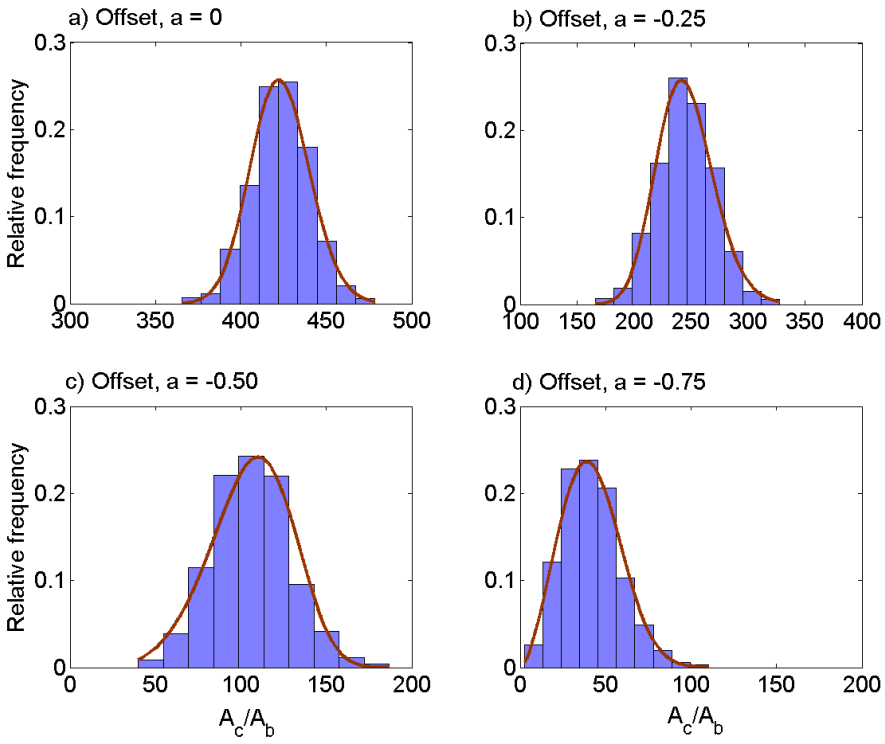

Fig. 4-11 Histogram of normalized lightning collection areas around a grounded structure of diameter, $D =$ 0.03 for a downward leader angle, $\theta_0 =$ 0 deg., and offset position at, a) $a =$ 0, b) $a =$ -0.25, c) $a =$ -0.5 and d) $a =$ -0.75.

Fig. 4-12 illustrates the variation in the lightning collection area for a grounded structure of a larger diameter, $D =$ 0.06, deployed at varying elevations above the ground surface for a leader propagating vertically downward. Again, the lightning collection area decreases with elevation of the structure above the ground surface, with the structure located closest to the thundercloud showing the largest collection area. Compared to a grounded structure of a smaller diameter discussed previously, the normalized lightning area for the structure with a larger diameter is reduced by approximately 4 times, which is the square of the ratio of the larger diameter and smaller diameter. This implies that the

reduction in the actual lightning collection area for the structure of larger diameter is minimal compared to that of the structure with a smaller diameter. In this case, the magnitude of the striking distance is not very sensitive to the diameter of the structure because the mean electrical potential gradient around the structure for both diameters, utilized in calculating the striking distance, either shows a slight variation or is similar in both cases.

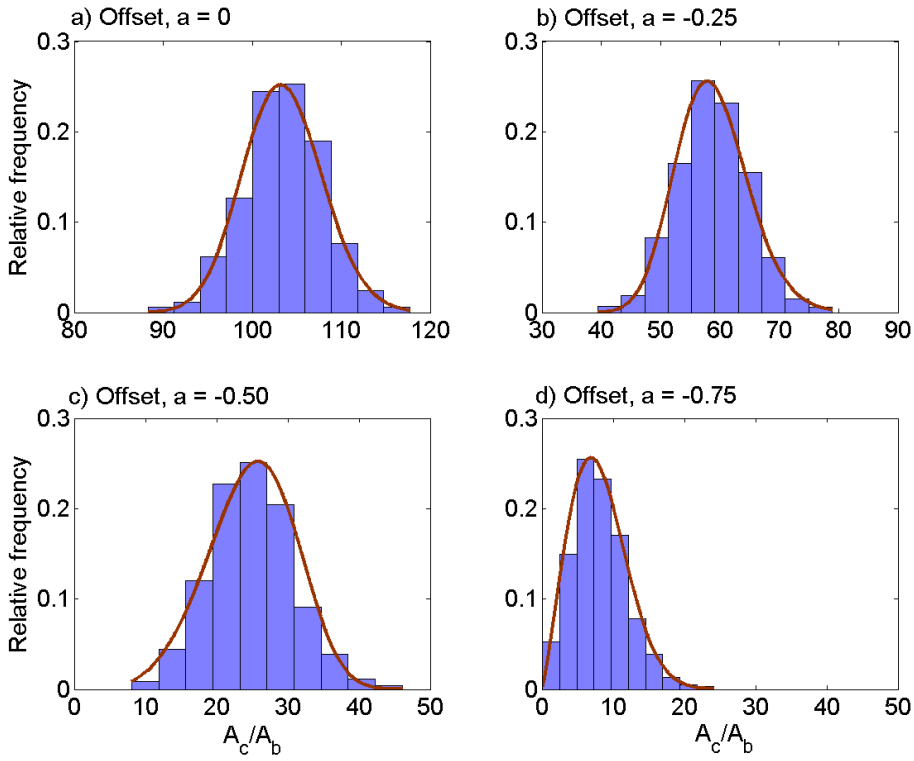

Fig. 4-12 Histogram of normalized lightning collection area around a grounded structure of diameter, $D =$ 0.06 for a downward leader angle, $\theta_0 =$ 0 deg., and offset position at, a) $a =$ 0, b) $a =$ -0.25, c) $a =$ -0.5 and d) $a =$ -0.75.

The effect of the angle of the downward leader on the lightning collection area around a grounded structure of diameter, $D = 0.03$ deployed at different elevations above the ground surface is illustrated in Fig 4-13. Considering a case of an oblique downward leader, the trends in the lightning collection area are similar to those observed for the vertically propagating downward leader discussed earlier, however, in this case the magnitude of the normalized lightning collection areas are reduced and the probability distributions are shifted to the left and the response is greatest for structures positioned at high elevations. These observations are attributed to the variation in the angular distribution of the potential field around a grounded structure. For a body deployed at a very high elevation, the potential field around the structure is predominately that from the thundercloud and the field varies largely with the angle on the outer surface of the structure. In contrast, a structure located close to the ground surface is surrounded by the potential field that is induced predominantly by the downward leader and the field shows minimal angular variation.

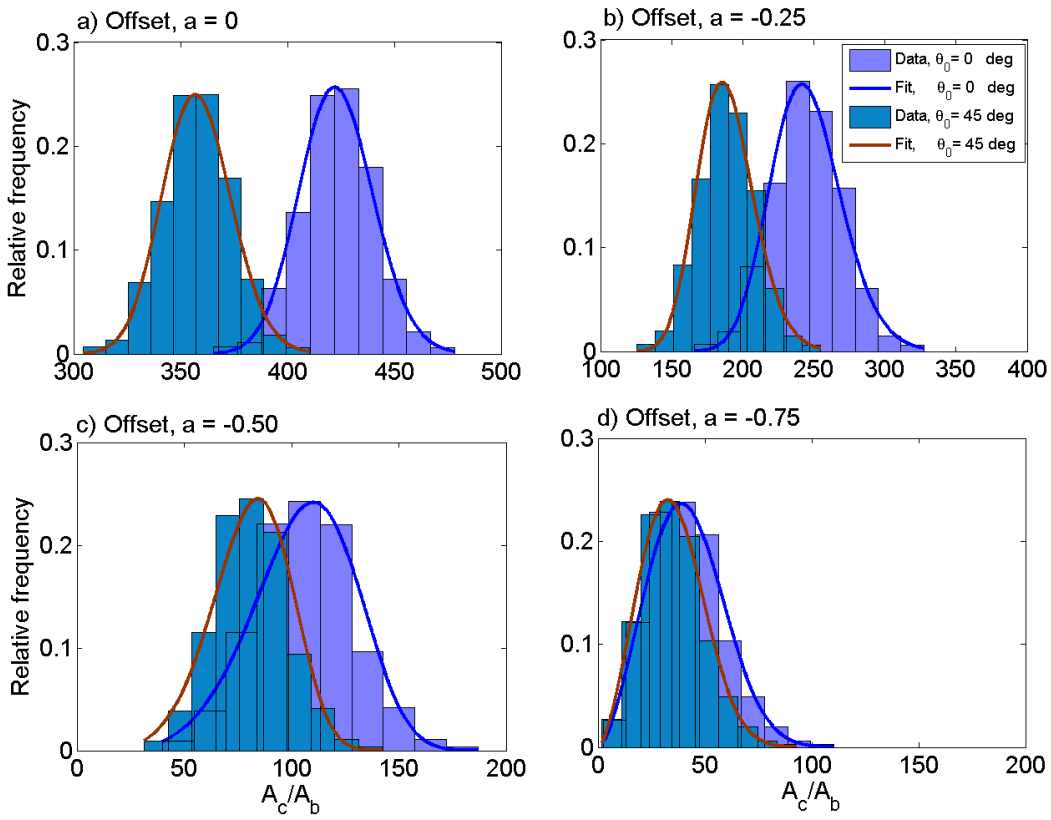

Fig. 4-13 Histogram of normalized lightning collection areas around a grounded structure of diameter, $D = 0.03$ for the downward leader angle, $\theta_0 = 0$ and 45 deg., and offset position at, a) $a = 0$, b) $a = -0.25$, c) $a = -0.5$, and d) $a = -0.75$.

The statistics of the lightning collection area around a grounded structure positioned at varying elevations above the ground surface for different downward leader angles are illustrated in Table 4-5. The mean lightning collection area around the structure, μ is largest in the case of the vertically propagating downward leader for all elevations of the grounded structure. The spread in the data, as illustrated by the standard deviation, σ is largest for the structure positioned at $a =$ -0.25 for both angles of the downward leader. The least spread in the data occurs for the structure located closest to the ground surface, for the oblique leader angle. The asymmetry in the probability distribution as illustrated by the skewness parameter, s_k is minimal for structures deployed at the highest elevations, that is offset distances, $a \geq$ -0.25. For the structures located at the offset distances, $a \leq$ -0.5, the asymmetry in the probability distribution is moderate, with the structure positioned closest to the ground surface showing the largest positive skew in the data, for both leader angles, implying that the data is shifted more towards the right direction. The asymmetry in the lightning collection area around the grounded structure positioned closest to the ground surface is probably attributed to the non-linearity in the striking distance associated with the dominant effect of the potential field contribution from the downward leader. Further, all the probability distribution functions of the lightning collection area, except that of the structure positioned closest to the ground surface, are close to Gaussian as shown by the kurtosis parameter, k_t. Similarly, the peakedness of the probability distribution of the lightning collection area for the structure located closest to the ground surface is probably attributed to the nonlinearity in striking distance for low elevations of the structure.

Table 4-5 Summary statistics of lightning collection area around a grounded structure of diameter, $D = 0.03$, deployed at varying elevations above the ground surface for different angles of the downward leader, θ_0.

Offset, a	$\theta_0 =$ 0 deg.				$\theta_0 =$ 45 deg.			
	μ	σ	s_k	k_t	μ	σ	s_k	k_t
0	423	17.1	-0.064	3.16	358	16.0	-0.041	3.16
-0.25	245	24.6	0.019	3.14	189	19.7	0.025	3.14
-0.50	106	22.6	0.190	3.16	81	17.1	0.200	3.17
-0.75	42	17.0	0.525	3.44	35	14.4	0.524	3.44

The frequency of negative lightning strikes to a grounded structure positioned at different elevations above the ground surface, for different angles of the downward leader are illustrated in Table 4-6. The ground flash density was assumed as $N_g = 6$ flashes/ km^2/year, a value within the range of the flash densities typically observed in the Central US and Gulf of Mexico (Orville et al., 2011). The mean frequency, N_{avg} and range, N_{rng} of downward negative lightning strikes to the grounded structure for downward leaders propagating vertically and at an oblique angle to the structure, decreases with the elevation of the structure above the ground surface, corroborating the trends in the potential field distribution and the corresponding lightning collection area, discussed earlier. Further, the mean frequency of the lightning strikes to the structure which moderately decreases with increase in the downward leader angle, exhibits behavior consistent with the distribution of lightning collection area.

Table 4-6 Summary statistics of the frequency of downward lightning strikes to a grounded structure of diameter, $D = 0.03$ deployed at varying elevation above the ground surface, for different downward leader angles, over a period of 5 years.

Offset distance, a	$\theta_0 = 0$ deg.		$\theta_0 = 45$ deg.	
	Mean, N_{avg}	Range, N_{rng}	Mean, N_{avg}	Range, N_{rng}
0	16.7	0.8 - 32.6	14.1	0.7 - 27.3
-0.25	9.4	0.5 - 16.7	7.2	0.4 - 12.7
-0.50	3.8	0.3 - 5.8	2.9	0.2 - 4.5
-0.75	1.4	0.2 - 1.7	1.1	0.1 - 1.4

5. SUMMARY AND CONCLUSIONS

A two-dimensional physics based model was developed to study the behavior of lightning in the near field of grounded elevated systems. The analysis envisions the field of interest as being enclosed within two non-concentric circles. The inner circle encompasses the body of interest and the periphery of the outer circle addresses the cloud coverage and ground surface. It is within this region that the total potential field solution, consisting of two contributions is determined. The total potential solution was first derived based upon an eigen-function expansion involving special functions. In order to address concerns identified regarding the numerical evaluation of leader propagation involving the second contribution to the total potential, a Green's function solution was derived as part of the model development.

The accuracy of the potential field between the non-concentric circles was investigated in order to develop a better understanding of the convergence and stability behavior of the potential field using established spectral concepts. It was found that the offset distance of the inner circle, and the truncation limit in the series expansions affected accuracy and numerical stability of the potential function. Both parameters define the pattern and conditioning of the coefficient matrix from the system of linear equations used to solve for the unknown coefficients. The condition number of the coefficient matrix was used to gauge the magnitude of error that arises from the solving the system of linear equations. Large condition numbers were considered a sign of ill-conditioned matrices, which can be difficult to solve without introducing significant error in the solution. The

stability analysis demonstrated that the optimal number of terms in the potential function decreases with inner circle offset distance along a band of condition numbers of similar magnitude and that increasing the truncation limit does not always lead to a better numerical solution.

This two-dimensional physics based model was validated using three different test cases having closed form solutions. Generally, the total potential field involving Green's function formulation for the second contribution to the total potential had lower relative error compared to the solution based on spherical Bessel functions. Further, it was observed that the magnitude of the error in the total potential field involving spherical Bessel functions showed a dependency on the diameter of the inner circle, with the largest error occurring at the boundaries of the inner and outer circles. In contrast, the magnitude of error in the potential field involving Green's function formulation remained relatively unchanged with increase in the diameter of the inner circle and the largest error in the potential field occurs in the region close to the outer boundary for all test cases considered. The accuracy of the total potential field of the lightning problem computed using the two different methods was compared and the results indicate that the potential field involving spherical Bessel functions shows increased spreading about the axis of the downward leader and can be considered accurate for practical applications in the case where the downward leader is distant from the structure while the field involving the Green's function is concentrated about axis of the downward leader and is accurate when the leader is close to the structure.

The behavior of the total potential field around a grounded structure and the corresponding distribution of upward leaders incepted from the surface of the structure was investigated with respect to the following key parameters, offset distance, size of structure, extent of cloud cover and downward leader angle. The distribution of the total potential field around the structure changes with elevation, and the magnitude of the potential field are greatest in the region close to the thundercloud. It was observed that the potential field was sensitive to the size of the structure enclosed by the inner circle. The regions of high risk to lightning strikes on the grounded structure are represented using the normal joint probability density function. The corresponding probability of lightning attachment on the surface of the structure increased with the elevation above the ground surface and decreased with increase in size of the structure, demonstrating a behavior consistent with the distribution of the potential field. The distribution of the total potential field around a structure was shown to change with the extent of the cloud cover, and the corresponding probability of lightning attachment on the structure increased with cloud size, again indicating behavior consistent with the distribution of the potential field. In addition, downward leaders propagating at oblique angles to the structure introduce asymmetry in the potential field altering the shape of the joint probability density function representing the region of high risk on the structure. Further, the largest allowable downward leader angle defines the extreme extent of the region of high risk on surface of the structure.

The total electrical charge induced on the perimeter of grounded structures of different shapes was estimated using the total potential field solution. The magnitude of

the electrical charge on the surface of the structure was shown to increase with elevation of the structure above the ground surface, with the largest electrical charge induced on a structure positioned closest to the thundercloud. Further, the potential field and the resulting surface electrical charge on the perimeter of the structure is a function of body shape. Slender structures highly perturb the ambient potential field leading to a large build-up of surface electrical charge on the structure. In contrast, broad structural shapes generate moderate potential gradients on perimeter of the structure yielding a lower surface electrical charge.

The electric charge dissipated during a lightning strike to a grounded structure was estimated using semi-empirical relationships. The charge from the long stroke process makes up the largest contribution of charge dissipated during a lightning strike to a ground structure. The estimates of the total charge computed in this study indicate that the design threshold for charge recommended for sizing lightning protection on grounded structures can be exceeded, implying that the design criteria can be inadequate in cases where large amounts of energy are dissipated through a grounded structure and therefore improvements in the criteria maybe warranted in these cases.

The lightning collection area around a grounded structure deployed at different elevations above the ground surface was investigated. The lightning collection area which is normalized by the area of the structure, was shown to increase with the elevation of the structure above the ground surface, and the structure positioned closest to the ground surface shows the smallest collection area. These trends are attributed to the variation in striking distance which decreases as the structure moves away from the region close to the

thundercloud where the ambient potential field and potential gradient on the surface of the grounded structure are greatest. Further, the impact of the diameter of the structure on lightning collection area was minimal since the threshold potential gradient used in calculating the striking distance varies slightly with the size of the grounded body. Further, the impact of the angle of the downward leader on the lightning collection area was investigated and results show that the collection area decreases with increase in leader angle, especially for structures deployed at high elevations due to the large angular variation of the potential field around the periphery of the structure. The frequency of downward negative lightning strikes to a grounded structure was shown to be a function of the elevation of the structure above the ground surface and angle of leader propagation indicating behavior consistent with the distribution of the potential field and the corresponding lightning collection area.

Despite the fact that this study addresses some of the limitations of earlier theoretical models, some challenges still exist. For example, the domain chosen for the model is limiting in the sense that, non-spherical shapes cannot be adequately treated, and the elevation and extent of the thundercloud is constrained by the size of the domain. In addition, the functions used to represent the current wave forms in the short stroke and long stroke processes may not adequately represent the temporal variation of electric current in nature and thus estimates of the charge dissipated during a lightning strike to a grounded structure, computed in this study can be considered approximate and subject to further study.

REFERENCES

Aeroscraft. (2014) "Products: Aeroscraft." http://www.aeroscraft.com. Cited 15 May 2014.

Ahrens, U., Diehl. M., and Schmehl. R. (2014). *Airborne Wind Energy*. Springer, New York, NY.

Altaeros. (2014). "Technology: BAT: The buoyant airborne wind turbine." http://www.altaerosenergies.com/bat.html. Cited on 15 March 2014.

Anderson, R. B., and Eriksson, A. J. (1980). "Lightning parameters for engineering application." Electra, 69, 65-102.

Ang, A. H., and Tang, W. H. (1975). *Probability Concepts in Engineering Planning and Design. Vol. 1- Basic Principles*. John Wiley & Sons, New York, NY.

Arfken, G. B., and Weber, H. J. (2005). *Mathematical Methods for Physicists, 6nd edition*. Academic Press, Charlottesville, VA.

Armstrong, H. R., and Whitehead, E. R. (1968). "Field and analytical studies of transmission line shielding." IEEE Transactions on Power Apparatus and Systems, 87(1), 270-281.

Asmar, N. H. (2005). *Partial Differential Equations with Fourier Series and Boundary Value Problems, 2nd edition*. Prentice Hall, Upper Saddle River, NJ.

Becerra, M., and Cooray, V. (2006). "A simplified physical model to determine the lightning upward connecting leader inception." IEEE Transactions on Power Delivery, 21(2), 897-908.

Becerra, M., Cooray, V., and Hartono, Z. A. (2007). "Identification of lightning vulnerability points on complex grounded structures." Journal of Electrostatics, 65, 562-570.

Becerra, M., Cooray, V., and Roman, F. (2008). “Lightning striking distance of complex structures.” IET General Transmission Distribution, 2(1), 131-138.

Berger, K. (1967). “Novel observations on lightning discharges: Results of research on Mount San Salvatore.” Journal of Franklin Institute, 283(6), 478-525.

Berger, K., Anderson, R. B., and Kroeninger, H. (1975). “Parameters of lightning flashes.” Electra, 41, 23-37.

Berkowitz, B., Lindeman, T., and Thorp, G. (2014). “Surveillance aircraft floating high above Maryland.” http://apps.washingtonpost.com/g/page/business/surveillance-aircraft-floating-high-above-maryland/752. Cited on 06 September 2014.

Bertelsen, K., Erichsen, H. V., Jensen, M. S., and Madsen, S. F. (2007). “Application of numerical models to determine lightning attachment points on wind turbines.” Proceedings of International Conference on Lightning and Static Electricity, Paris France.

Bondiou, A., and Gallimberti, I. (1994). “Theoretical modeling of the development of the positive spark in long gaps.” Journal of Physics D Applied Physics, 27(6), 1252-1266.

Borse, G. J. (1997). *Numerical methods with Matlab. A Resource for Scientists and Engineers.* PWS Publishing Company, Boston, MA.

Brodkin, J. (2013). “Google flies internet balloons in stratosphere for a network in the sky. Project Loon: Solar-powered balloons beam internet down to Earth.” http://www.arstechnica.com. Cited 15 May 2014.

Cooray, V., Rakov, V., and Theethayi, N. (2007). “The lightning strike distance-revisited.” Journal of Electrostatics, 65, 296-306.

Cooray, V., and Becerra, M. (2012). “Attractive radii of vertical and horizontal conductors evaluated using a self-consistent leader inception and propagation model-SLIM.” Atmospheric Research, 117, 64-70.

Eriksson, A. J. (1978). “Lightning and tall structures.” Transactions of the South African Institute of Electrical Engineers, 69(8), 238-252.

Fagiano, L., Milanese, M., and Piga, D. (2010). “High altitude wind power generation.” IEEE Transactions of Energy Conversion, 25(1), 168-180.

Fletcher, C. A., and Roberts. B.W. (1979). “Electricity generation from jet stream winds.” Journal of Energy, 3(4), 241-249.

Furuya, O., and Maekawa. S. (1984). “Technical and economic assessment of tethered wind energy systems.” Journal of Solar Engineering, 106, 327-334.

Goelian, N., Lalande, P., Bondiou-Clergerie, A., Bacchiega, G. L., Gazzani, A., and Gallimberti, I. (1997). “A simplified model for the simulation of positive-spark development in long air gaps.” Journal of Physics D, Applied Physics, 30(17), 2441-2452.

Golde, R. H. (1978). “Lightning and tall structures.” Proceedings of IEEE, 125(4), 347-351.

Google. (2014a). “Project Loon: Loon for all, balloon-powered internet for everyone.” http://www.google.com/loon/. Cited 08 August 2014.

Google. (2014b). “Advanced wind energy: Airborne wind turbines.” http://www.google.com/makani/. Cited 08 August 2014.

Hewitt E., and Hewitt, R. E. (1979). “The Gibbs-Wilbraham phenomenon: an episode in Fourier analysis.” Archive for History of Exact Sciences, 21(2), 129-160.

International Electrotechnical Commission (IEC). (2010a). *IEC 61400-24 Standard, Wind Turbines-Part 24: Lightning Protection*. IEC Press, Geneva, Switzerland.

IEC. (2010b). *IEC 62305-1 Standard, Protection Against Lightning - Part 1: General Principles*. IEC Press, Geneva, Switzerland.

Jackson, J. D. (1999). *Classical Electrodynamics*. John Wiley & Sons, Inc., Hoboken, NJ.

Ji, Y., and He. J. (2013). "Analysis on lightning triggering possibility along transmission tethers of high altitude wind energy exploitation system." Electric Power Systems Research, 94, 16-23.

Krider, E. P., and Guo, C. (1983). "The peak electromagnetic power radiated by lightning return strokes." Journal of Geophysical Research, 88, 8471-8474.

Krider, E. P. (1986). *Physics of Lightning, Studies in Geophysics: The Earth's Electrical Environment*. National Academy Press, Washington, DC.

Lai, M., Lin, W., and Wang, W. (2002). "A fast spectral-difference method without pole conditions for Poisson-type equations in cylindrical and spherical geometries." IMA, Journal of Numerical Analysis, 22, 537-548.

Lai, M., and Tseng, J. (2007). "A formally fourth-order accurate compact scheme for 3D Poisson equation in cylindrical and spherical geometries." White paper, National Chiao Tung University, Taiwan.

MacRobert, T. M. (1967). *Spherical harmonics; an elementary treatise on harmonic functions with applications.* Pergamon Press, New York, NY.

Madsen, S. F., and Erichsen, H.V. (2009). "Numerical model to determine lightning attachment point distributions on wind turbines according to the revised IEC 61400-2." Proceedings of the International Conference on Lightning and Static Electricity, Pittsfield MA.

Madsen, S. F., Bertelsen, K., Krogh, T.H., Erichsen, H.V., Hansen, A. N., and Lonbaek, K. B. (2012). "Proposal of new zoning concept considering lightning protection of wind turbine blades." Journal of Lightning Research, 4(2), 108-117.

Miyake, K., Suzuki, T., Takashima, M., Takuma, M., and Tada, T. (1990). "Winter lightning on Japan sea coast: Lightning striking frequency to tall structures." IEEE Transactions on Power Delivery, 5(3), 1370-1376.

Miyake, K., Suzuki, T., and Shinjou, K. (1992). "Characteristics of winter lighting current on Japan Sea Coast." IEEE Transactions on Power Delivery, 7(3), 1450-1457.

Morse, P. M., and Feshbach, H. (1953). *Methods of Theoretical Physics, Vol., 2*. McGraw Hill Company, New York, NY.

National Oceanic and Atmospheric Administration (NOAA). (2014). "National Buoy Data Center." http://www.ndbc.noaa.gov. Cited 15 May 2014.

O' Doherty, R. J., and Roberts, B.W. (1981). "The application of U.S upper wind data in design of tethered wind energy systems." Report Number, SERI/TR-211-1400. Solar Energy Research Institute, Golden, CO.

Orville, R. E. (1968). "A high speed time-resolved spectroscopic study of lightning return stroke." Journal of Atmospheric Science, 25, 827-856.

Orville, R. E., Huffines, G. R., Burrows, W. R., and Cummins, K. L. (2011). "The North American Lightning Detection Network (NALDN) - Analysis of flash data: 2001-2009." Monthly Weather Review, 139, 1305-1322.

Paolella, M. S. (2006). *Fundamental Probability: A Computational Approach*. John Wiley & Sons, Hoboken, NJ.

Raytheon. (2014). "Joint Land Attack Cruise Missile Defense Elevated Netted Sensor System". http://raytheon.com. Cited 08 September 2014.

Rakov, V.A., and Uman, M. A. (2003). *Lightning Physics and Effects*. Cambridge University Press, Cambridge, United Kingdom.

Reese, O. W. (1971). "Numerical method and Fortran program for solving Poisson's equation over axisymmetric regions of a sphere." Technical Note, NASA TN D-6438. National Aeronautics and Space Administration, Langley, VA.

Riegler. G., and Riedler. W. (1983). "Transformation of wind energy by a high altitude power plant." Journal of Energy, 7(1), 92-94.

Riegler. G., and Riedler. W. (1984). “Tethered wind systems for the generation of electricity.” Journal of Solar Engineering, 106, 177-181.

Rizk, F. M. (1994). “Modeling of lightning incidence to tall structures. Part I: Theory.” IEEE Transactions on Power Delivery, 9(1), 162-170.

Roberts, B., Shepard, D., Caldeira, K., Cannon, M., Eccles, D., and Grenier, A. (2007). “Harnessing high-altitude wind power.” IEEE Transaction on Energy Conversion, 22, 136–144.

Roberts, J., and Roberts, T. D. (1978). “Use of the Butterworth low-pass filter for oceanographic data.” Journal of Geophysical Research, Oceans, 83(C11), 5510-5514.

Saba, M. F., Schultz, W., Warner, T. A., Campos, L. Z., Schumann, C., Krider, E. P., Cummins, K. L., and Orville, R. E. (2010). “High-speed video observations of positive lightning flashes to ground.” Journal of Geophysical Research, 115, 1-9.

Schonland, B. J. (1964). *The Flight of Thunderbolts*. Clarendon Press, Oxford, United Kingdom.

Sorensen, T., Brask, M. H., Grabau, P., and Olsen, K. (1998). “Lightning damages to power generation wind turbines.” Proceedings of International Conference of Lightning Protection, Birmingham, United Kingdom

Szedenik, N. (2001). “Rolling sphere.” Journal of Electrostatics, 51, 345-350.

Trefethen, L. N. (1992). “Pseudospectra of matrices.” Proceedings of the Biennial Conference on Numerical Analysis, Dundee Scotland, Griffiths DF, Watson GA, eds., Longman Scientific and Technical, Essex, United Kingdom.

Trefethen, L. N., and Embree, M. (2005. *Spectra and Pseudospectra: The Behavior of Non-normal*. Princeton University Press, Princeton, NJ.

Uman, M. A. (1969). *Lightning*. McGraw Hill, New York, NY.

Uman, M. A., and Rakov, V. A. (2003). “The interaction of lightning with airborne vehicles.” Progress in Aerospace Sciences, 39, 61-81.

Vermilion. C., and L. Fagiano. (2013). “Electricity in the air: tethered wind energy systems.” ASME Control and Dynamics Magazine, 1(3), 13-21.

Wright, T. G. (2002). “Eigtool: A graphical tool for non-symmetric eigenvalue problems.” http://web.comlab.ox.ac.uk/projects/pseudospectra/software.html. Cited 15 June 2013.

APPENDIX A

Coordinate Transformation

The general solution to the Laplace with Dirichlet boundary conditions and Poisson equation with zero boundary data can be rewritten in terms of coordinates of the inner circle after transforming coordinates of the outer circle. The radii and angles of the inner circle are given as r_1 and θ_1, respectively. On the other hand, the radii and angles of the outer circle are given as r_2 and θ_2, respectively. The distances in the triangle OPR, as illustrated in Fig. A1, in coordinates of the inner circle are given by the form

$$\begin{aligned} OP &= r_1 \sin\theta_1 \\ \Delta a &= r_1 \cos\theta_1 \\ a + \Delta a &= a + r_1 \cos\theta_1 \end{aligned} \tag{47}$$

Also from triangle OPQ, the same distances can rewritten in coordinates of the outer circle as given by the form

$$\begin{aligned} OP &= r_2 \sin\theta_2 \\ a + \Delta a &= r_2 \cos\theta_2 \end{aligned} \tag{48}$$

Relating Equations 47 and 48, enables coordinates of the outer circle to rewritten in terms of coordinates of the inner circle as given by the form

$$\begin{aligned} r_2 \sin\theta_2 &= r_1 \sin\theta_1 \\ r_2 \cos\theta_2 &= a + r_1 \cos\theta_1 \end{aligned} \tag{49}$$

Solving for the radius of the outer circle, r_2 by squaring both sides of Eq. (49) leads to the following form

$$\begin{aligned} r_2^2 \sin^2\theta_2 &= r_1^2 \sin^2\theta_1 \\ r_2^2 \cos^2\theta_2 &= a^2 + 2ar_1 \cos\theta_1 + r_1^2 \cos^2\theta_1 \end{aligned} \tag{50}$$

Solving Eq. 50 and grouping like terms and noting that

$$\sin^2\theta + \cos^2\theta = 1 \tag{51}$$

leads to an expression for radius of the outer circle in terms of the coordinates of the inner circle as given by the form

$$\begin{aligned} r_2^2\left[\sin^2\theta_2 + \cos^2\theta_2\right] &= a^2 + 2ar_1\cos\theta_1 + r_1^2\left[\sin^2\theta_1 + \cos^2\theta_1\right] \\ r_2^2 &= a^2 + 2ar_1\cos\theta_1 + r_1^2 \end{aligned} \tag{52}$$

The corresponding expression for θ_2 is given by the form

$$\theta_2 = \cos^{-1}\left[\frac{a + r_1\cos\theta_1}{r_2}\right] \tag{53}$$

Similarly, the coordinates of the inner circle can be expressed as function of the offset distance and coordinates of the outer circle as given by the following form

$$\begin{aligned} r_1^2 &= r_2^2 - 2ar_2\cos\theta_2 + a^2 \\ \theta_1 &= \cos^{-1}\left[\frac{r_2\cos\theta_2 - a}{r_1}\right] \end{aligned} \tag{54}$$

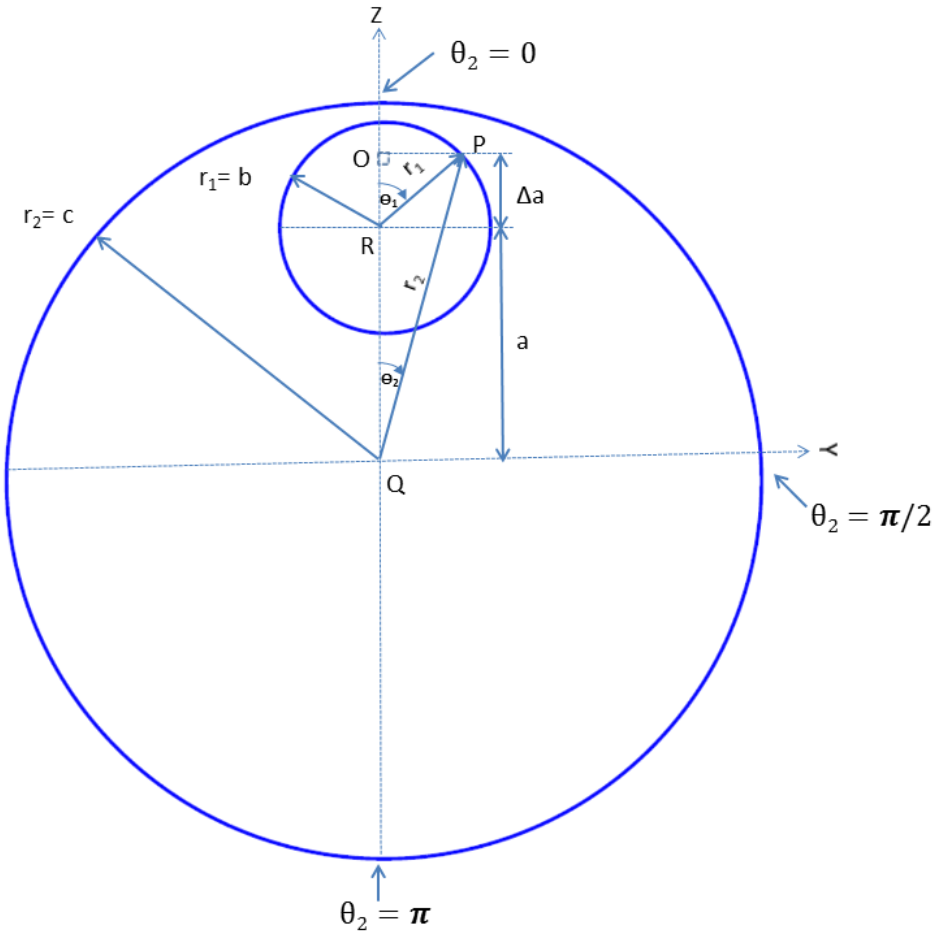

Fig. A-1 Geometry of non-concentric circles with axial symmetry about the vertical axis.

Translation Theorem

The translation of components of the general solution of the Laplace equation written in coordinates of the inner circle can be rewritten in terms of the coordinates of the outer circle utilizing the following expression for the translation theorem (Morse and Feshbach, 1953)

$$
\begin{aligned}
(r_1)^n P_n(\cos\theta_1) &= a^n \sum_{s=0}^{n} \left[\frac{(-1)^{n-s} n!}{s!(n-s)!} \right] \left(\frac{r_2}{a} \right)^s P_s(\cos\theta_2) \\
\left(\frac{1}{r_1} \right)^{(n+1)} P_n(\cos\theta_1) &= \left(\frac{1}{a} \right)^{(n+1)} \sum_{s=n}^{N} \left[\frac{s!}{n!(s-n)!} \right] \left(\frac{a}{r_2} \right)^{s+1} P_s(\cos\theta_2)
\end{aligned}
\tag{55}
$$

where, r_1 is the radius of inner circle, θ_1 is the zenith angle in coordinates of inner circle, r_2 is the radius of outer circle, θ_2 is the zenith angle in coordinates of outer circle, a is the distance between the centers of the inner and outer circle along the vertical axis, n and s are summation indices, $P_n(.)$ and $P_s(.)$ are Legendre functions.

APPENDIX B

Probability Density Distributions

The probability density functions for the different type of distribution illustrated in the numerical examples include the log-normal, Weibull and bivariate normal probability distributions. The log normal probability density function, $f(x)$ is given by the form (Ang and Tang, 1975)

$$f(x) = \frac{1}{x\sigma\sqrt{2\pi}} \exp\left[-\frac{1}{2}\left(\frac{In\, x - \mu}{\sigma} \right)^2 \right], \qquad x = [0, \infty] \tag{56}$$

where, x is a random variable, μ and σ are the mean and standard deviation of the logarithm of the random variable, respectively.

The Weibull probability density function, $f(x; \beta, x_0, \alpha)$ is given by the following form (Paolella, 2006)

$$f(x; \beta, x_0, \alpha) = \frac{\beta}{\alpha}\left(\frac{x - x_0}{\alpha} \right)^{\beta - 1} \exp\left[-\left(\frac{x - x_0}{\alpha} \right)^{\beta} \right], \quad x = [0, \infty] \tag{57}$$

where, x is a random variable, x_0 and α are location and scale parameters, respectively and β is a shape parameter.

The bivariate normal density function, $f(x, y)$ is given by the form (Ang and Tang, 1975)

$$f(\mathrm{x}, \mathrm{y}) = \frac{1}{2\pi\sigma_x\sigma_y\sqrt{1-\rho^2}} \exp\left[-\frac{1}{2\left(1-\rho^2\right)} \left\{ \left(\frac{x-\mu_x}{\sigma_x} \right)^2 - 2\rho\left(\frac{x-\mu_x}{\sigma_x} \right)\left(\frac{y-\mu_y}{\sigma_y} \right) + \left(\frac{y-\mu_y}{\sigma_y} \right)^2 \right\} \right. \tag{58}$$

where, x and y are random variables with a range, $x=[-\infty,\infty]$; $y=[-\infty,\infty]$. The mean of x and y variables are given as μ_x and μ_y, respectively. The corresponding standard deviation is given as σ_x and σ_y, respectively. The correlation coefficient between the x and y random variables is given as, ρ.